TU Delft

Delft University of Technology

Inertial effects in sedimenting suspensions of solid spheres in a liquid

Shajahan, Tariq; Breugem, Wim Paul

DOI
10.1016/j.ijmultiphaseflow.2023.104498

Publication date
2023

Document Version
Final published version

Published in
International Journal of Multiphase Flow

Citation (APA)
Shajahan, T., & Breugem, W. P. (2023). Inertial effects in sedimenting suspensions of solid spheres in a liquid. *International Journal of Multiphase Flow*, *166*, Article 104498. https://doi.org/10.1016/j.ijmultiphaseflow.2023.104498

Important note
To cite this publication, please use the final published version (if applicable).
Please check the document version above.

Copyright
Other than for strictly personal use, it is not permitted to download, forward or distribute the text or part of it, without the consent of the author(s) and/or copyright holder(s), unless the work is under an open content license such as Creative Commons.

Takedown policy
Please contact us and provide details if you believe this document breaches copyrights.
We will remove access to the work immediately and investigate your claim.

This work is downloaded from Delft University of Technology.
For technical reasons the number of authors shown on this cover page is limited to a maximum of 10.

International Journal of Multiphase Flow 166 (2023) 104498

Contents lists available at ScienceDirect

International Journal of Multiphase Flow

journal homepage: www.elsevier.com/locate/ijmulflow

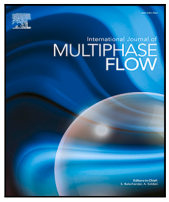

Inertial effects in sedimenting suspensions of solid spheres in a liquid

Tariq Shajahan, Wim-Paul Breugem *

Laboratory for Aero & Hydrodynamics, Process & Energy Department, Delft University of Technology, Mekelweg 2, 2628 CD Delft, The Netherlands

ARTICLE INFO

Dataset link: https://doi.org/10.4121/1cc98fd6-8d50-4203-96c0-125020c4c242

Keywords:
Sedimentation
Wake trapping
Drafting–kissing–tumbling
Particle interactions
Kinematic waves

ABSTRACT

Particle-resolved Direct Numerical Simulations have been performed on the gravitational settling of monodisperse solid spheres in a viscous fluid and triply periodic domain. In a comprehensive study, the bulk solid volume concentration was varied from $\phi = 0.5$ to 30%. To study the effect of inertia, three different Galileo numbers were considered in the inertial regime, $Ga = 144$, 178 and 210, for which a single settling sphere exhibits distinctly different wake and path characteristics. The particle/fluid mass density ratio was fixed at 1.5. We find that for $\phi = 2 - 30\%$ the suspension microstructure and dynamics depend predominantly on the bulk concentration. In qualitative agreement with previous studies in literature, three different sedimentation regimes can be distinguished: (1) the dilute concentration regime for $\phi \lesssim 2\%$ with preferential settling of particles in vertical trains, (2) the moderate concentration regime for $2\% \lesssim \phi \lesssim 10\%$ with preferential settling of particles in horizontal pairs with an interparticle distance of ~ 1.5 particle diameters, and (3) the dense concentration regime for $\phi \gtrsim 10\%$ with a nearly random ("hard-sphere") distribution of the particles in space. The clustering of particles is dictated by, respectively, trapping of particles in the wake of other particles, a drafting–kissing–tumbling (DKT) instability by which two vertically aligned particles quickly reorient themselves into a horizontally aligned particle pair, and short-range multiparticle interactions through viscous lubrication and to a lesser extent collisions between particles. In all cases, hindered settling at a reduced speed is observed as compared to a single settling sphere. The well-known Richardson–Zaki relation for the mean sedimentation velocity appears valid only for the dense concentration regime. We provide ample evidence that in the dense regime the characteristic velocity and time scales of particle motion are proportional to $\sqrt{gD_p}$ and $\sqrt{D_p/g}$, respectively, with g the gravitational acceleration and D_p the particle diameter. We also observe an ω^{-3} scaling of the particle velocity spectra for $\omega\sqrt{D_p/g} \gtrsim 0.4$ and we propose a model to explain this scaling behavior, based on the inertial response of the particles to small-scale flow perturbations. Kinematic waves, i.e., vertically propagating plane waves in the local concentration field, are observed in all cases, though unrelated particle motions are responsible for significant loss of the spatio-temporal coherence of the waves. The wave speed was determined from repeated space–time autocorrelations of the local concentration field and appears in reasonable agreement with Kynch sedimentation theory using the Richardson–Zaki relation. The passage of kinematic waves causes perturbations in the particle velocity at a frequency that matches well with peak frequencies in the particle velocity spectra for concentrations up to $\phi \approx 10\%$. The time-lagged cross-correlation of the vertical and horizontal particle velocity suggests that kinematic waves may trigger DKT instabilities, while conversely DKT instabilities may be responsible for the onset of kinematic waves. Finally, we suggest that obstruction and perturbation of the particle wake by neighboring particles could offer an explanation for the small influence of the Galileo number on the suspension behavior for $\phi = 2 - 30\%$.

1. Introduction

Sedimentation refers to the collective settling of particles under gravity or centrifugal forces. It is a commonly occurring process in nature and many industrial applications. Examples are deposition of sediments in rivers, sedimentation of volcanic ash, rainfall, settling basins in waste water treatment, land reclamation through spraying large amounts of sediments in, e.g., sea, and blood separation centrifuges. Sedimentation is also closely related to fluidization, where an upward fluid flow exerts a hydrodynamic force on the particles such that their average settling velocity is zero and which has many applications in chemical industry. Provided that wall effects can be neglected and the particles are homogeneously fluidized, the two processes are dynamically similar, having the same relative particle/fluid

* Corresponding author.
E-mail address: W.P.Breugem@tudelft.nl (W.-P. Breugem).

https://doi.org/10.1016/j.ijmultiphaseflow.2023.104498
Received 25 February 2023; Received in revised form 17 April 2023; Accepted 20 April 2023
Available online 3 May 2023
0301-9322/© 2023 The Author(s). Published by Elsevier Ltd. This is an open access article under the CC BY license (http://creativecommons.org/licenses/by/4.0/).

velocity when the fluidization velocity (flow rate divided by the cross-sectional area of the fluidization column) is equal to the average particle settling velocity in sedimentation (Richardson and Zaki, 1954; Barnea and Mizrahi, 1973). For many applications, it is desired to accurately predict the sedimentation or fluidization velocity as function of particle concentration. For fluidized bed reactors, a homogeneous spatial particle distribution and strong fluid and particle mixing are typically desired too.

A large body of sedimentation literature has focused on sedimentation of small particles in the Stokes regime (Davis and Acrivos, 1985; Phillips et al., 1988; Ladd, 1993; Guazzelli and Hinch, 2011; Hamid et al., 2013). The complex particle–fluid and multi-particle interactions are responsible for chaotic particle behavior and limit a detailed analytical treatment of the problem except for very dilute sphere suspensions (Batchelor, 1972; Batchelor and Wen, 1982). Sedimentation of larger particles in the inertial regime (i.e., at a Reynolds number $Re_T > O(1)$, based on the terminal settling velocity and diameter of a single settling particle) has received comparatively less attention. The presence of inertial effects not only increases the complexity of the flow physics, detailed and well-controlled experiments are particularly challenging in this regime and it puts severe requirements on computational methods for accurate simulation of sedimentation. However, the development of efficient methods for particle-resolved simulations (Prosperetti and Tryggvason, 2009; Maxey, 2017) and the ever increasing computing power have recently paved the way to study the influence of inertia on sedimentation in great detail.

In the present study we consider sedimentation of non-colloidal suspensions of spheres in a viscous and Newtonian fluid for which molecular forces such as Van der Waals and electrostatic forces as well as Brownian motion can be neglected. That is, we consider particle diameters $\gg 1\,\mu$m and a large Péclet number related to Brownian particle motion (Guazzelli and Morris, 2012). From dimensional analysis it can be shown that the sedimentation dynamics of non-colloidal suspensions in free (unbounded) space is governed by the following three dimensionless numbers: (1) the Galileo number, $Ga = v_g D_p/\nu_f$, with $v_g = \sqrt{|\rho_p/\rho_f - 1|gD_p}$ the inertio-gravitational velocity, ρ_p the particle mass density, ρ_f the fluid mass density, g the gravitational acceleration, D_p the particle diameter, and ν_f the fluid kinematic viscosity, (2) the particle-to-fluid mass density ratio, ρ_p/ρ_f, and (3) the bulk solid volume fraction, ϕ. In literature, sometimes the terminal Reynolds number of a single settling particle is used instead of Ga to characterize the relative importance of fluid inertia over viscous forces and the two numbers are related to each other through $Re_T = \left(2/\sqrt{3C_d}\right) Ga$ with $C_d = C_d(Re_T)$ the sphere drag coefficient.

The seemingly simple case of a single sphere settling in free space exhibits already rich physics as has been explored in a number of comprehensive numerical studies (Jenny et al., 2004; Zhou and Dušek, 2015; Auguste and Magnaudet, 2018) and extensive experimental campaigns (Veldhuis and Biesheuvel, 2007; Horowitz and Williamson, 2010; Raaghav et al., 2022). While for $Ga \lesssim 155$, a sphere settles steadily in the vertical direction once it has reached its terminal velocity and exhibits an axi-symmetric wake, at $Ga \approx 155.6$ ($Re_T \approx 206.1$) and irrespective of the particle-to-fluid density ratio, the sphere wake undergoes a regular bifurcation and becomes planar symmetric (Fabre et al., 2012), causing the particle to steadily rotate and settle down at a small inclination angle of a few degrees with respect to the vertical (Zhou and Dušek, 2015). Upon further increasing the Galileo number, different transition scenarios exist dependent on the density ratio and thus on the influence of the fluid/solid coupling strength on the translational and rotational sphere dynamics (Auguste and Magnaudet, 2018). At a density ratio around 1, the sphere undergoes a secondary Hopf bifurcation, displaying an oscillating oblique path and periodic vortex shedding from the wake. The wake then becomes irregular and transitions into a chaotic state for $Ga \gtrsim 200$, with the sphere settling on average in the vertical again, and with evidence of an intermediate periodic (vertical oscillating) state for $250 \lesssim Ga \lesssim 300$ (Zhou and Dušek, 2015; Raaghav et al., 2022).

The collective settling of particles is generally characterized by hindered settling, i.e., a reduced settling speed with respect to a single settling particle. This originates on the one hand from the higher mixture mass density and thus larger Archimedes force, and on the other hand from the enhanced hydrodynamic drag on a particle from the nearby presence of other particles and the upward return flow of the fluid (Barnea and Mizrahi, 1973). Hindered settling has already been studied over more than 80 years and many empirical correlations have been proposed (Barnea and Mizrahi, 1973; Garside and Al-Dibouni, 1977; Davis and Acrivos, 1985). Richardson and Zaki (1954) proposed a simple correlation that is widely used:

$$V_s = kV_T(1-\phi)^n\,, \tag{1}$$

where V_T is the terminal settling velocity of a single particle in free space, $n = n(Re_T, D_p/D_{pipe})$ with D_{pipe} the diameter of the sedimentation tube, and $k = 1$ for sedimentation and $log_{10}(k) = -D_p/D_{pipe}$ for fluidization. (The difference in k value between sedimentation and fluidization was attributed to the presence of a liquid velocity gradient near the wall in the latter; the presence of a wall breaks the similarity between the two processes.) Based on their experimental data, Richardson and Zaki proposed correlations for n, varying from $n = 4.65$ for the Stokes regime and when wall effects are negligible to $n = 2.39$ for $Re_T > 500$.

Theoretical support for Eq. (1) has been provided by Batchelor (1972) who derived that $k = 1$ and $n = 6.55$ for a very dilute, statistically homogeneous and monodisperse suspension in the Stokes regime, while $n \approx 5.6$ when the spheres are slightly bidisperse in size at high Péclet number based on the relative sphere settling velocity (Batchelor and Wen, 1982; Davis and Birdsell, 1988). Garside and Al-Dibouni (1977) critically evaluated Eq. (1) and proposed a single correlation for n, which varies from 5.1 for the Stokes regime down to 2.7 for the high-Reynolds regime. Moreover, they reported that Eq. (1) deviates from experimental data for concentrations below 10%, an effect most pronounced for the higher Reynolds number range. Here it should be noted that Richardson and Zaki actually did not do measurements for $\phi < O(5\%)$, but fitted Eq. (1) to the dense regime to determine n and kV_T, and divided the latter by a theoretical estimate of V_T to determine k.

The deviation of Eq. (1) from data for the dilute regime was noticed in many later studies (Yin and Koch, 2007; Felice, 1999; Zaidi et al., 2015; Shajahan and Breugem, 2020), with the deviation increasing for decreasing ϕ and increasing Re_T. Interestingly, based on particle-resolved simulations for $Re_T \simeq 1-20$ and $\rho_p/\rho_f = 2$, Yin and Koch (2007) attributed the deviation for $\phi \lesssim 5\%$ to anisotropy of the suspension microstructure caused by inertial wake interactions between spheres, while the suspension microstructure was isotropic and exhibited a "hard-sphere" particle distribution (Wertheim, 1963; Guazzelli and Morris, 2012) for $\phi \gtrsim 5\%$ where Eq. (1) gave a good fit. The wake interaction between vertically oriented pairs of spheres was explained by a drafting–kissing–tumbling (DKT) phenomenon (Fortes et al., 1987; Wu and Manasseh, 1998; Jayaweera et al., 1964) present at finite Reynolds number. Shielded in the wake of the leading particle, the trailing particle experiences less drag and accelerates towards the leading particle ("drafting"), while simultaneously it experiences a shear-induced lift force (Koch, 1993). When this lift force is not strong enough, the particles will eventually touch ("kissing"). Either way, irrespective whether actual contact is made or not, the particles will quickly move from a highly unstable vertical to a horizontal pair orientation and repel each other horizontally ("tumbling"). Yin and Koch suggested that particle tumbling is hindered by the nearby presence of other particles, explaining the observed enhanced likelihood of particle pairs to orient themselves horizontally at a distance of 2–2.5 particle diameters for $\phi = 1$ and 5% at $Re_T = 10$, while the prevalence of chaotic multi-particle interactions may explain the observed isotropic

microstructure for $\phi = 20\%$. A similar tendency for horizontal particle alignment at moderate concentrations and an isotropic particle distribution for the dense regime was observed in later studies (Zaidi et al., 2014; Hamid et al., 2014; Willen and Prosperetti, 2019; Seyed-Ahmadi and Wachs, 2021).

Compared to the isotropic microstructure in the dense regime, the enhanced drag from prevalent horizontal particle pairs in the lower concentration range may explain the steeper decrease in the sedimentation velocity with increasing concentration than expected from Eq. (1) (Hamid et al., 2014). Consistent with this, Yin and Koch found $k \approx 0.86$–0.92, which is thus smaller than $k = 1$ suggested by Richardson and Zaki but in agreement with $k \approx 0.8$–0.9 found from experiments (Di Felice and Parodi, 1996; Felice, 1999) and particle-resolved simulations (Willen et al., 2017; Willen and Prosperetti, 2019; Shajahan and Breugem, 2020). Based on literature data and additional simulations for $Ga = 4.6$–153.6 and $\rho_p/\rho_f = 1.3$–6, Yao et al. (2021) recently proposed a correlation of k in the form of an exponentially decaying function in Ga^2, which varies from $k = 0.89$ for $Ga \to 0$ to $k = 0.7$ for $Ga = 153.6$. They attributed the drop in k with increasing Ga to the influence of Ga on the frequency and lifespan of clusters that were quantified by means of Voronoï tessellation. The change in cluster formation was associated with appreciable particle wake interactions for the lowest Ga and the dominance of collisions over wake interactions for the highest Ga investigated.

Contrary to hindered settling, in several studies an increase in the settling speed has been reported for very dilute suspensions when Ga is sufficiently high (Kajishima and Takiguchi, 2002; Kajishima, 2004; Uhlmann and Doychev, 2014; Zaidi et al., 2014; Huisman et al., 2016; Fornari et al., 2016b; Seyed-Ahmadi and Wachs, 2021). This was first observed in particle-resolved simulations by Kajishima and Takiguchi (2002) for $\phi = 0.2\%$, $Re_T = 350$ and 400 ($Ga \approx 243$ and 272) and $\rho_p/\rho_f = 8.8$ and 10, respectively, though particle rotation was ignored in their study for computational reasons. The enhanced settling speed was related to the formation of elongated vertical clusters with a lateral extent of $\sim 10D_p$ and a life time of several particle response times. They attributed the formation of clusters to wake trapping of particles in the unsteady wakes of other particles and the breakup of clusters to turbulent stresses that are intensified by the presence of clusters. Finally, their results suggest a threshold Reynolds number of around 200 ($Ga \approx 154$) for vertical cluster formation and enhanced settling. In a follow-up study, Kajishima (2004) studied the effect of particle rotation and concentration on cluster formation at $Re_T = 300$ ($Ga \approx 214$) and $\rho_p/\rho_f = 8.8$. When rotation is accounted for, no vertical clusters were formed at $\phi = 0.05\%$, while clusters and an enhanced settling speed of $\sim 20\%$ was observed for $\phi = 0.1$–0.4%. Furthermore, particle rotation was responsible for a shorter lifetime and irregular formation of clusters, which was attributed to the rotation that particles obtain in the high shear zones surrounding the clusters and the resulting Magnus lift force that tends to expel particles from the clusters.

The results of Kajishima and Takiguchi (2002) and Kajishima (2004) were corroborated by particle-resolved simulations of Uhlmann and Doychev (2014) for $Ga = 121$ and 178, $\rho_p/\rho_f = 1.5$ and $\phi = 0.5\%$. While particles were nearly randomly distributed in space for $Ga = 121$ and settled on average at approximately the same speed as a single settling particle, elongated vertical clusters with a lateral extent of $\sim 10D_p$ were formed for $Ga = 178$ and the average settling speed was enhanced by about 12%. They attributed the formation of these vertical clusters to particle wake attraction related to the DKT mechanism, though Yin and Koch (2007) invoked the same DKT mechanism to explain the reduced likelihood of finding vertical particle pairs and the higher likelihood of finding horizontal particle pairs in their simulations at lower Ga and higher ϕ. Based on the critical Ga for transition of the wake and path of a single settling sphere from axisymmetric and vertical to plane symmetric and oblique, Uhlmann and Doychev (2014) conjectured that the threshold Galileo number for the emergence of the vertical clusters is approximately 155 related to the enhanced likelihood of particles to encounter each other when they are settling in an oblique fashion. Experimental evidence of vertical cluster formation and enhanced settling was provided by Huisman et al. (2016) for $Ga = 110$–310, $\rho_p/\rho_f = 2.5$ and $\phi = 0.02$–0.1% with a maximum speed increment of 25% found for $Ga = 170$ and $\phi = 0.05\%$. Contrary to the conjecture of Uhlmann and Doychev (2014) also an enhanced settling speed of up to 19% was found for $Ga = 110$, though Huisman et al. noted that their results may have been biased by the presence of a large-scale flow circulation induced by the settling of the particles in the middle of their settling tank. Particle-resolved simulations by Zaidi et al. (2014) showed significantly enhanced settling for $\phi = 0.5$ and 1%, $\rho_p/\rho_f = 2.5$ and $Re_T \geq 175$. The latter condition corresponds to $Ga \geq 138$, thus well below 155.

From the above literature discussion, it is clear that flow inertia may have a profound effect on the suspension microstructure and the flow dynamics, in particular in the lower concentration range. Compared to the moderate Ga regime, only few studies have yet addressed the effect of flow inertia for $Ga > 100$ for a wide range in ϕ, see the overview of particle-resolved Direct Numerical Simulation (DNS) studies of the inertial regime in Table 1.

In a previous study for $Ga = 144$, $\rho_p/\rho_f = 1.5$ and ϕ varying from 0.5%–30% (Shajahan and Breugem, 2020), we observed three different settling regimes with a different suspension microstructure: a dilute concentration regime for $\phi \lesssim 1\%$, a moderate concentration regime for $1 \lesssim \phi \lesssim 10\%$, and a dense concentration regime for $\phi \gtrsim 10\%$, with a preference of particles to settle in vertically aligned clusters, horizontally aligned pairs and a nearly isotropic fashion, respectively. Little is yet known about how the microstructure and related flow dynamics will change when increasing Ga and how this will affect the transition between flow regimes when the concentration is varied. In the present study, we aim to gain understanding of the structure and dynamics of sedimenting suspensions by (1) examining the competing influences of wake trapping, drafting–kissing–tumbling and multiparticle interactions, and (2) examining the influence of inertia by varying Ga for a wide range of concentrations. Partially motivated by earlier studies of Uhlmann and Dušek (2014) and Uhlmann and Doychev (2014), we have chosen 3 different Galileo numbers, $Ga = 144$, 178 and 210, at a fixed density ratio of $\rho_p/\rho_f = 1.5$. For a single settling particle in free space, these values are a priori expected to correspond to a steady vertical settling path at $Ga = 144$ with $Re_T \approx 184$, a steady oblique settling path at $Ga = 178$ and $Re_T \approx 240$, and an oscillating oblique or chaotic settling path at $Ga = 210$ and $Re_T \approx 293$ (Zhou and Dušek, 2015).

For our study, we employed particle-resolved DNS to simulate sedimentation of spheres in a triply periodic computational domain at $\phi = 0.5$–30% and the chosen Ga values. The case of $\phi = 0.5\%$ was simulated only for $Ga = 144$ as to check whether or not vertical particle clustering would result in an enhanced settling speed in this case as Uhlmann and Doychev (2014) suggested that $Ga \gtrsim 155$ is required for this. The lowest concentration considered for $Ga = 178$ and 210 is $\phi = 2\%$ as the focus of the present study is primarily on the moderate and dense concentration regime. The DNS is based on an Immersed Boundary Method for the fluid/solid coupling (Breugem, 2012) in combination with a soft-sphere collision model for frictional particle collisions (Costa et al., 2015). A few results for $Ga = 144$ from our previous study (Shajahan and Breugem, 2020) are included in the present study for the sake of comparison with the other Ga.

We present results for the suspension microstructure by means of particle-conditioned averages, particle statistics such as the mean and root-mean-square (rms) velocities of the particles and fluid phase, probability density functions (pdfs) of the particle velocity, and particle velocity correlations and related frequency (energy) spectra. We also examine the role of particle collisions by analyzing the particle force balance. Finally, we analyze the properties of so-called kinematic waves (Kynch, 1952; El-Kaissy and Homsy, 1976; Batchelor, 1988;

Table 1
Overview of the investigated parameter ranges in particle-resolved DNS studies of fluidization and sedimentation in free space (no walls) of non-colloidal monodisperse spheres in the inertial regime ($Ga \gg 1$). Studies are ordered by the highest investigated Ga value. When Ga was not provided in the reference, it was estimated from Re_T using Abraham's empirical correlation for the drag coefficient (Abraham, 1970), and vice versa when only Ga was provided.

Literature reference	Ga	Re_T	ϕ (in %)	ρ_p/ρ_f
Climent and Maxey (2003)	1.4–18.1	0.1–10	0.3–12	0.9-5
Hamid et al. (2014)	0.97–18.1	0.05–10	1–40	5
Yin and Koch (2008)	2.0–28.3	0.2–20	1, 20	2
Yin and Koch (2007)	4.6–28.5	1–20	0.5–40	2
Zaidi et al. (2015)	1.4–53.4	0.1–50	0–40	2.5[a]
Esteghamatian et al. (2017)	59.4	57.9	∼ 47	10
Willen et al. (2017), Willen and Prosperetti (2019)	49.7–99.4	43.3–110.8	8.7–34.9	2-5
Shajahan and Breugem (2020)	144	185.9	0.5–30	1.5
Fornari et al. (2016b)	144.9	188	0.5, 1	1.02
Yao et al. (2021)	4.6–153.6	0.95–200.0	22–43	1.3-6
Seyed-Ahmadi and Wachs (2021)	70, 160	72.4, 210.3	1–20	2
Uhlmann and Doychev (2014)	121, 178	141.6, 260.6	0.5	1.5
Fornari et al. (2016a)	19–200	10.8–276.5	0.5	1.02
Zaidi et al. (2014)	4.7–214.0	1–300	0.5–5	2.5
Kajishima (2004)	214.0	300	0.05–0.4	8.8
Zaidi (2018)	3.2–272.2	0.5–400	1–20	2.5[a]
Kajishima and Takiguchi (2002)	53.4–272.2	50–400	0.2	8.8, 10
Present study	144–210	185.9–290.4	0.5–30	1.5

[a]Density ratio was not explicitly mentioned, but presumed here to be 2.5 based on earlier publication of the same lead author.

Kytömaa and Brennen, 1991; Jackson, 2000), i.e., vertically propagating plane waves in the local concentration with a relatively small amplitude, which we observed before in our previous study for $Ga = 144$ (Shajahan and Breugem, 2020). Recently, Willen et al. (2017) analyzed the characteristics of kinematic waves in DNS of a homogeneously fluidized bed for $Ga = 50$–99, $\rho_p/\rho_f = 2$–5 and $\phi = 8.7$–34.9%. The wave speed was found to be in good agreement with Kynch theory (Kynch, 1952) in combination with the Richardson–Zaki correlation, Eq. (1), for the sedimentation velocity. Based on a truncated spatial Fourier series reconstruction, they demonstrated the footprint of propagating concentration waves on the vertical fluid velocity. In the present study we will adopt a different method to analyze kinematic waves based on repeated space–time autocorrelations of the local concentration field, which avoids the need to apply filtering in wavenumber space. Fortes et al. (1987, p. 468) suggested that particle aggregation associated with DKT interactions may cause propagation of 'voidage cracks' in fluidization and we will explore this idea in the present sedimentation study with regard to kinematic waves.

The remainder of this manuscript is organized as follows. In Section 2 we provide details on the computational method and setup used in the DNS. In Section 3 we present results for a single settling sphere at the three chosen Galileo numbers. In Section 4 the results are discussed for sedimenting suspensions. Finally, in Section 5 we summarize the conclusions and provide a discussion of our main findings.

2. Computational setup

2.1. Governing equations and collision model

The physics of the fluid phase and the particle dynamics are governed by the Navier–Stokes and Newton–Euler equations, respectively. We use the following inertial scales to non-dimensionalize these equations: $l_{ref} = D_p$, $u_{ref} = \sqrt{gD_p}$, $t_{ref} = l_{ref}/u_{ref}$, $p_{ref} = \rho_f u_{ref}^2$ and $a_{ref} = u_{ref}^2/l_{ref}$. The non-dimensional Navier–Stokes equations for an incompressible and Newtonian fluid are then given by:

$$\nabla \cdot \mathbf{u}_f = 0\,, \tag{2a}$$

$$\frac{\partial \mathbf{u}_f}{\partial t} + \nabla \cdot \mathbf{u}_f\mathbf{u}_f = -\nabla p_h - \nabla p + \frac{1}{\sqrt{gD_p^3/\nu_f^2}}\nabla^2\mathbf{u}_f\,, \tag{2b}$$

where $\mathbf{u}_f$ is the fluid velocity and p is the total fluid pressure excluding the contributions from the weight per unit volume of the fluid and the net weight per unit volume of the suspended particles, p_h. Note that $\sqrt{gD_p^3/\nu_f^2} = Ga/\sqrt{\rho_p/\rho_f - 1}$. The gradient of p_h is equal to $\nabla p_h = \left(\rho_p/\rho_f - 1\right)\phi\,\tilde{\mathbf{g}}$, where $\tilde{\mathbf{g}}$ is a dimensionless unit vector pointing in the direction of gravity. The linear velocity, $\mathbf{u}_p$, and the angular velocity, $\boldsymbol{\omega}_p$, of a particle are described by the Newton–Euler equations, which for non-colloidal solid spheres are given by:

$$\left(\frac{\rho_p}{\rho_f}\frac{\pi}{6}\right)\frac{d\mathbf{u}_p}{dt} = \oint_{A_p}\boldsymbol{\tau}_f\cdot\mathbf{n}\,dA + \frac{\pi}{6}\left(\frac{\rho_p}{\rho_f} - 1\right)(1-\phi)\,\tilde{\mathbf{g}} + \mathbf{F}_c\,, \tag{3a}$$

$$\left(\frac{\rho_p}{\rho_f}\frac{\pi}{60}\right)\frac{d\boldsymbol{\omega}_p}{dt} = \oint_{A_p}\mathbf{r}\times(\boldsymbol{\tau}_f\cdot\mathbf{n})\,dA + \mathbf{T}_c\,, \tag{3b}$$

where $\boldsymbol{\tau}_f$ is the stress tensor for a Newtonian fluid defined as $\boldsymbol{\tau}_f = -p\mathbf{I} + \left(1/\sqrt{gD_p^3/\nu_f^2}\right)(\nabla\mathbf{u}_f + \nabla\mathbf{u}_f^T)$ with $\mathbf{I}$ the unit tensor, $\mathbf{r}$ is the position vector relative to the centroid of the particle, $\mathbf{n}$ is the outward-pointing unit normal on the particle surface (A_p), and $\mathbf{F}_c$ and $\mathbf{T}_c$ are the collisional force and torque, respectively. Eqs. (2a)–(3b) are coupled with each other through the no-slip/no-penetration condition at the surface of the particles:

$$\mathbf{u}_f = \mathbf{u}_p + \boldsymbol{\omega}_p\times\mathbf{r} \quad \text{at } \mathrm{A}_p\,. \tag{4}$$

Collisions between particles are modeled using a frictional soft-sphere collision model described in detail by Costa et al. (2015). In this model the rigid particles are allowed numerically to overlap slightly. A linear spring–dashpot model is used in which the collision force is computed from the overlap and relative velocity between the particles. The model accounts for transition from the stick to the slip regime dependent on the ratio of the tangential to the normal component of the collision force. The spring stiffness and damping coefficients for the normal and tangential collision force components are expressed in terms of four model parameters (van der Hoef et al., 2006): the dry normal and tangential (or rotational) coefficients of restitutions, $e_{n,dry}$ and $e_{t,dry}$, respectively, the Coulomb coefficient of sliding friction, μ_c, and the collision duration, T_c. Joseph and Hunt (2004) experimentally determined that $e_{n,dry} = 0.97$, $e_{t,dry} = 0.39$ and $\mu_c = 0.15$ for the oblique impact of a glass particle on a thick Zerodur (glass-like) wall in both air and an aqueous glycerine solution. We took the same values for our collision parameters with the exception of $e_{t,dry}$, which was set to 0.1; the lower value effectively promotes transition to the slip regime. The collision duration is a numerical parameter. In order to accurately resolve collisions in time, it was artificially stretched to $T_c = 8\Delta t$ with Δt the computational time step (Costa et al., 2015).

As will be explained in Section 2.2, the present DNS makes use of a fixed Cartesian grid for the fluid phase. Hydrodynamic interactions between particles are resolved as long as the distance between particle interfaces is larger than $O(\Delta x)$ with Δx the grid spacing; the associated interaction force and torque are included in the first term at the right-hand side of Eqs. (3a) and (3b), respectively. For distances smaller than the grid spacing, the normal interaction force between particles is increasingly underestimated as the flow in the intervening gap between the particles is not sufficiently resolved anymore. To compensate for this, a lubrication correction force is added to the right-hand side of Eq. (3a) when the distance between particle interfaces drops below a grid-dependent threshold value. The correction is based on an asymptotic analytical expression for the lubrication force for the normal approach between two equal solid spheres in the Stokes regime (Costa et al., 2015; Dance and Maxey, 2003). As the analytical correction force approaches infinity in the limit of zero gap width, the diverging behavior is capped when the gap width drops below a threshold distance of $5{\cdot}10^{-4}D_p$, which can be associated with the typical height of roughness asperities on the surface of the particles (Joseph and Hunt, 2004).

2.2. Numerical method, initialization and flow parameters

The DNS is based on the computationally efficient Immersed Boundary Method (IBM) of Breugem (2012) for the particle/fluid coupling, which is a modified version of the original IBM introduced by Uhlmann (2005). The IBM makes use of two different grids: a fixed Eulerian grid for the fluid phase and a Lagrangian grid on the surface of every particle and moving with the particle. A key ingredient of the IBM is that the no-slip/no-penetration condition given by Eq. (4), is not imposed in a direct manner, but forces are added locally near the particle's surface to enforce this condition by good approximation. The additional IBM force, $\mathbf{f}$, is added to the right-hand side of the fluid momentum Eq. (2b). The present IBM falls in the class of direct-forcing methods (Fadlun et al., 2000) and is embedded in the predictor–corrector scheme used to integrate the Navier–Stokes equations. The force is calculated using a regularized delta-function approach in which the regularized delta function proposed by Roma et al. (1999) is used to first interpolate the provisional fluid velocity from the Eulerian to the Lagrangian grid, then the IBM force is computed on the Lagrangian grid such that the corrected velocity will fulfill the no-slip/no-penetration condition, and finally the IBM force is spread back from the Lagrangian to the Eulerian grid using the same regularized delta function. From the force distribution on the Lagrangian grid, the overall hydrodynamic force and torque acting on the particle are computed. The IBM contains a multi-direct forcing scheme (Luo et al., 2007) to reduce the error in the enforced no-slip/no-penetration condition caused by overlapping interpolation kernels from neighboring Lagrangian grid points. Furthermore, the Lagrangian surface grid is slightly retracted towards the interior of the particle over a distance of $0.3\Delta x$ to compensate for the finite width of the interpolation kernels. This improves the accuracy of the overall method. The reader is referred to Breugem (2012) for further details and validation of the present IBM.

The three-step Runge–Kutta method of Wray (Wesseling, 2001) is used to integrate the Navier–Stokes and Newton–Euler equations in time. The computational time step, Δt, is dynamically adjusted to ensure numerical stability. The Navier–Stokes equations are discretized in space on a fully staggered Cartesian grid. The central-differencing scheme is used to approximate spatial gradients. The computational domain is a triply periodic rectangular box. Gravity is acting in the negative y-direction.

At the start of the simulations, the particles are randomly placed in the domain subject to the criterion that they must not overlap with each other. The particles and fluid phase are initialized with zero velocity. When the particles start to fall downwards by the action of gravity, a return fluid flow co-develops by virtue of the imposed hydrostatic pressure gradient in Eq. (2b). Within a few tens of time units $\sqrt{D_p/g}$, the flow reaches a statistically steady state in which the average particle velocity is slightly fluctuating in time around a constant value. The imposed hydrostatic pressure gradient then balances the submerged weight of the suspension and the overall mixture (fluid+particles) velocity is zero. The zero bulk mixture velocity mimics the virtual presence of a bottom wall as in a batch sedimentation process. The statistics shown later in this manuscript have been calculated for $t > 50\sqrt{D_p/g}$ to ensure that a statistically steady state was reached in all simulations.

Table 2
Physical parameters and computational settings used in the present parametric DNS study: Ga is the Galileo number, ϕ is the global solid volume fraction, N_p is the number of particles in the computational domain, $L_x \times L_y \times L_z$ are the dimensions of the computational domain, $D_p/\Delta x$ is a measure for the grid resolution, and T_{obs} is the duration of the observation interval over which statistics were obtained.

Ga	ϕ	N_p	$L_x \times L_y \times L_z$	$D_p/\Delta x$	$T_{obs}/\sqrt{D_p/g}$
144	0.005	2686	$37.5D_p \times 200D_p \times 37.5D_p$	16	2157
	0.02	2388	$25D_p \times 100D_p \times 25D_p$	16	2134
	0.04	4775	$25D_p \times 100D_p \times 25D_p$	16	1036
	0.06	7163	$25D_p \times 100D_p \times 25D_p$	16	1046
	0.08	9549	$25D_p \times 100D_p \times 25D_p$	16	1060
	0.10	11936	$25D_p \times 100D_p \times 25D_p$	16	1060
	0.15	17903	$25D_p \times 100D_p \times 25D_p$	16	1143
	0.20	23871	$25D_p \times 100D_p \times 25D_p$	16	1154
	0.25	29838	$25D_p \times 100D_p \times 25D_p$	16	1144
	0.30	35806	$25D_p \times 100D_p \times 25D_p$	16	1134
178	0.02	2388	$25D_p \times 100D_p \times 25D_p$	24	1367
	0.04	4775	$25D_p \times 100D_p \times 25D_p$	24	684
	0.06	7163	$25D_p \times 100D_p \times 25D_p$	24	706
	0.08	9549	$25D_p \times 100D_p \times 25D_p$	24	727
	0.10	11936	$25D_p \times 100D_p \times 25D_p$	24	735
	0.15	17903	$25D_p \times 100D_p \times 25D_p$	24	753
	0.20	23871	$25D_p \times 100D_p \times 25D_p$	24	745
	0.25	29838	$25D_p \times 100D_p \times 25D_p$	24	731
	0.30	35806	$25D_p \times 100D_p \times 25D_p$	24	729
210	0.02	2388	$25D_p \times 100D_p \times 25D_p$	24	983
	0.06	7163	$25D_p \times 100D_p \times 25D_p$	24	673
	0.10	5968	$25D_p \times 50D_p \times 25D_p$	24	693
	0.20	11936	$25D_p \times 50D_p \times 25D_p$	24	693
	0.25	14919	$25D_p \times 50D_p \times 25D_p$	24	768
	0.30	17903	$25D_p \times 50D_p \times 25D_p$	24	713

As mentioned in the introduction section, we performed a parametric study in which we varied the Galileo number and the bulk solid volume fraction. The particle-to-fluid mass density ratio was fixed at a value of 1.5. In total 25 different sedimentation cases have been simulated. The simulation parameters are listed in Table 2.

Note that the domain height in case A1 was set to 200 particle diameters, which is 2–4 times larger than in the other cases. This was done for two reasons. Firstly, to improve convergence of particle statistics by increasing the number of particles in the domain for this case with the lowest bulk concentration. Secondly, to accommodate large-scale columnar structures present at this bulk concentration (Shajahan and Breugem, 2020). We checked *a posteriori* for all cases that the domain height was much larger than the estimated vertical distance over which fluctuations in the vertical particle velocity are decorrelated, see Shajahan and Breugem (2020) where a prior analysis is presented for $Ga = 144$. A higher grid resolution was used for $Ga = 178$ and 210 than for $Ga = 144$, in order to sufficiently resolve the flow field at the higher Galileo and hence higher Reynolds numbers. The chosen grid resolutions for the different Galileo numbers were motivated by a previous numerical study of Uhlmann and Dušek (2014) in which they analyzed the grid sensitivity of their DNS/IBM results for gravitational settling of a single particle at the same density ratio and for a similar range in Galileo number as considered in the present study. The grid resolution of the Lagrangian grid was chosen to match as closely as possible the resolution of the Eulerian grid, corresponding to 746 and 1721 Lagrangian grid cells for $D_p/\Delta x = 16$ and 24, respectively.

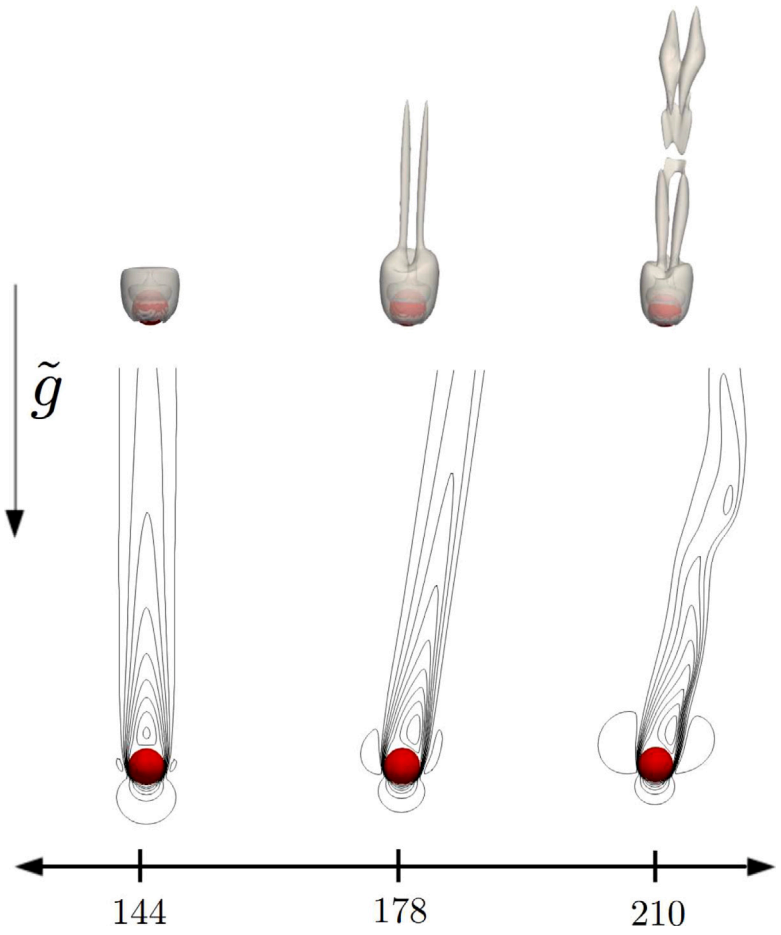

Fig. 1. Visualization of the instantaneous flow field around a single particle settling in free space for $Ga = 144$, 178 and 210. Top panels show the $\lambda_2 = -0.015$ isocontour of the λ_2 vortex identification criterion (Jeong and Hussain, 1995). Bottom panels show isocontours of the relative fluid velocity ranging from $-0.2\sqrt{gD_p}$ to $1.0\sqrt{gD_p}$ (see main text for a more detailed explanation).

3. Single settling particle in free space

For each investigated Galileo number, an additional simulation was performed of a single settling particle in free space to determine the terminal settling velocity of an individual particle and to validate the DNS code. The size of the rectangular computational domain and the grid resolution are listed in Table 3. Prescribed inflow and convective outflow boundary conditions were applied in the vertical y-direction and periodic boundary conditions were imposed in the horizontal x and z directions. The initial centroid position of the particle was set to $x = L_x/2$, $y = 9D_p$ and $z = L_z/2$. A moving frame of reference was used in which the inflow velocity was set slightly higher than the expected terminal settling velocity of the particle. This was done in order to track the particle motion over a sufficiently long time to capture the development of possible wake and sphere path instabilities. Following the procedure used by Uhlmann and Dušek (2014), during the first part of the simulation the particle was fixed in space till the flow around the particle was fully developed. Then the simulation was restarted and the particle was allowed to move freely during the second part of the simulation. The terminal settling velocity was determined from the difference between the vertical particle drift velocity and the prescribed inlet velocity.

Similar to Uhlmann and Dušek (2014), Fig. 1 shows visualizations of the fully developed flow field around the freely settling particle for each Galileo number. The top panels show visualizations in terms of the λ_2 vortex identification criterion (Jeong and Hussain, 1995). For the vertical plane passing through the particle centroid and parallel to the particle velocity, the bottom panels show isocontours of the vertical fluid velocity relative to the particle. At $Ga = 144$ the particle falls steadily downwards along the vertical and exhibits an axisymmetric wake. At $Ga = 178$ the particle settles steadily along a slightly oblique trajectory at an angle of approximately 7.1° with the vertical. The wake is no longer axisymmetric, but plane symmetric, and contains two characteristic vortex threads. Consistent with the presence of a skewed wake, the particle rotates steadily along a horizontally aligned axis with an angular velocity of approximately $0.052\sqrt{g/D_p}$ (in the clockwise direction for the plane shown in Fig. 1). Finally, at $Ga = 210$ the particle shows periodic wake shedding with an oscillation period of $7.3\sqrt{D_p/g}$. This is accompanied by a small periodic oscillation of the inclination angle at which the particle is falling, varying in the range of 9.6–9.9°. The flow visualizations for $Ga = 144$ and 178 are in good agreement with the numerical results presented by Uhlmann and Dušek (2014) for the same Galileo numbers based on spectral/spectral-element simulations and simulations based on an IBM similar to the one presently used. Minor differences can be attributed to differences in domain size, grid resolution, boundary conditions and accuracy of the methods used. The case of $Ga = 210$ was not investigated by them, but they did simulate the case of $Ga = 190$, which exhibits similar oscillatory behavior.

For all three Galileo numbers, the values for the terminal settling velocity, $V_T/\sqrt{gD_p}$, and the corresponding terminal Reynolds number, $Re_T = |V_T|D_p/\nu_f$, are shown in Table 3. Good agreement is found with the results from the spectral/spectral-element simulations of Uhlmann and Dušek (2014) for $Ga = 144$ and 178. The table also includes the expected terminal Reynolds number from the balance between the submerged weight of the particle and the steady hydrodynamic

Table 3
Computational settings, terminal settling velocity and terminal Reynolds number obtained from DNS of a single settling particle with a particle-to-fluid density ratio of 1.5. Ga is the Galileo number, $L_x \times L_y \times L_z$ is the domain size, $D_p/\Delta x$ is a measure for the grid resolution, $V_T/\sqrt{gD_p}$ is the normalized terminal settling velocity in the vertical direction, and Re_T is the terminal settling Reynolds number. The last three columns show Re_T obtained from, respectively, the present DNS, the spectral/spectral-element simulations of Uhlmann and Dušek (2014) for their largest domain size, and the expected values using Abraham's correlation for the drag coefficient (Abraham, 1970).

Ga	$L_x \times L_y \times L_z$	$D_p/\Delta x$	$V_T/\sqrt{gD_p}$	Re_T (present)	Re_T (from Uhlmann and Dušek, 2014)	Re_T (model Abraham, 1970)
144	$22D_p \times 30D_p \times 22D_p$	16	−0.913	185.9	185.1	184.5
178	$22D_p \times 30D_p \times 22D_p$	24	−0.953	239.8	243.0	239.8
210	$22D_p \times 30D_p \times 22D_p$	24	−0.978	290.4	–	293.3

drag force using Abraham's empirical correlation for the drag coefficient (Abraham, 1970). Again, good agreement is found for all Ga values, which demonstrates the accuracy of our simulations for the chosen grid resolutions.

4. DNS results for sedimenting suspensions

4.1. Instantaneous spatial particle distribution

Snapshots of the instantaneous spatial particle distribution are shown in Fig. 2 for $\phi = 6\%$, 20% and 30% for each investigated Galileo number. For a compact representation, only part of the flow domain is shown ($25D_p \times 50D_p \times 6.25D_p$). The particles are colored by their instantaneous vertical velocity normalized with the mean sedimentation velocity, V_s. A discrete colorbar is used to distinguish between four groups of particles: particles settling at a velocity higher than the mean with $v_p/V_s > 1.25$ (red color), particles settling around the mean in the range of $0.75 < v_p/V_s < 1.25$ (yellow), particles settling at a velocity less than the mean with $0 < v_p/V_s < 0.75$ (blue), and particles moving in the upward direction, $v_p/V_s < 0$ (green).

The snapshots clearly show that in all cases a large number of particles settle at a velocity significantly lower or higher than the mean. Also, the slower and faster moving particles are seemingly segregated in space and contained in relatively large-scale structures with a spatial dimension $\gg D_p$. A small amount of particles appears to move even in the upward direction. The relative fraction of upward moving particles increases with increasing bulk concentration as will be analyzed in more detail in Section 4.5. This likely originates from a locally strong return flow of the fluid, which may drag some particles along in the upward direction. Hydrodynamic particle interactions and particle bouncing after collisions might also cause individual particles to move instantaneously upward. Finally, we remark that no clear effect of the Galileo number can be discerned from the snapshots in contrast with the Ga-dependent wake dynamics of a single settling particle discussed in the previous section. For a more in-depth analysis of particle clustering and effects of Ga on this, we present results for the suspension microstructure by means of the particle-conditioned average concentration and flow field in the next subsection.

4.2. Suspension microstructure

The particle-conditioned average (PCA) concentration field has been computed in the same way as in our previous study (Shajahan and Breugem, 2020). First, we computed the spatial distribution of the instantaneous solid phase indicator function around each particle, $\gamma(\mathbf{x}-\mathbf{x}_c,t)$, in two mutually perpendicular and vertically oriented planes passing through the particle centroid at $\mathbf{x}_c(t)$. Here we define γ as the local solid volume fraction in a grid cell, which varies between 0 for cells located fully inside the fluid phase and 1 for cells contained fully inside particles. The 2D spatial distributions of γ were then averaged over all particles and time, and, because of statistical symmetry, also over the two mutually perpendicular planes to obtain the PCA concentration field, $\overline{\gamma}(\mathbf{x}-\mathbf{x}_c)$, where the bar denotes the statistical average. A similar procedure was used to compute the PCA relative particle and fluid velocity fields, defined by $\overline{\gamma[\mathbf{u}_p(\mathbf{x}-\mathbf{x}_c,t)-\mathbf{u}_p(\mathbf{x}_c,t)]}/\overline{\gamma}$ and $\overline{(1-\gamma)[\mathbf{u}_f(\mathbf{x}-\mathbf{x}_c,t)-\mathbf{u}_p(\mathbf{x}_c,t)]}/\overline{(1-\gamma)}$, respectively.

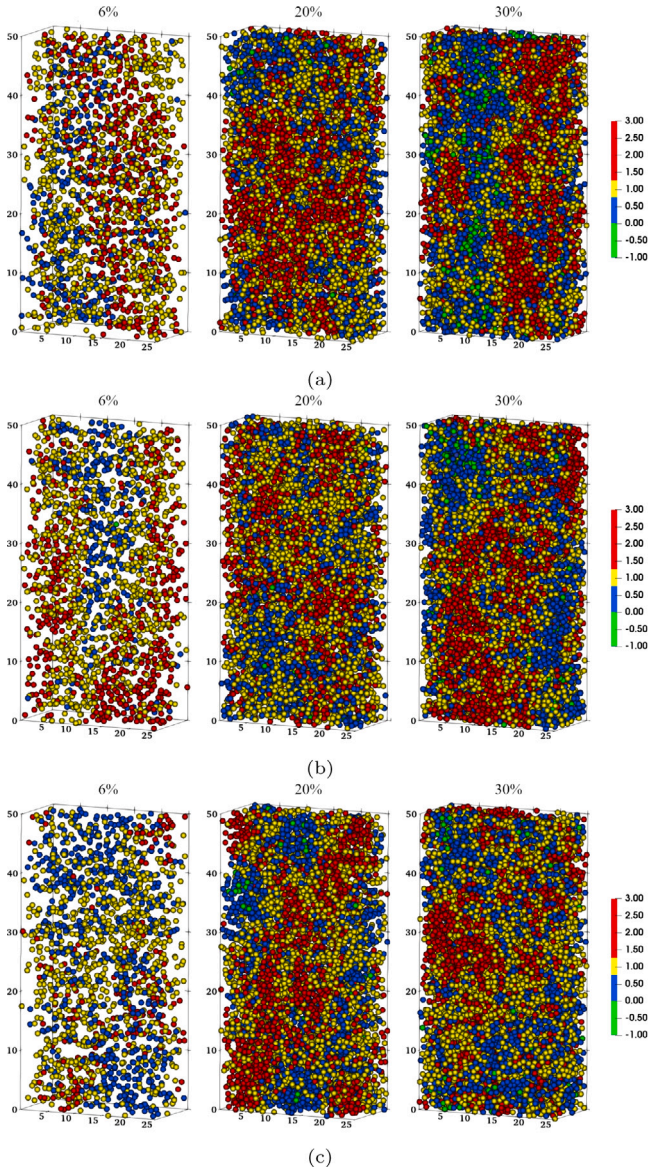

Fig. 2. Instantaneous snapshots of the spatial particle distribution in sedimenting suspensions as function of Galileo number and bulk concentration (indicated by the numbers on top of the panels). The particles are colored by their vertical velocity normalized with the mean sedimentation velocity, v_p/V_s. Note that $v_p > 0$ (upward moving particle) corresponds to $v_p/V_s < 0$ as $V_s < 0$. (a) $Ga = 144$, (b) $Ga = 178$, (c) $Ga = 210$. (For interpretation of the references to color in this figure legend, the reader is referred to the web version of this article.)

Fig. 3 presents the PCA concentration field in the vertical plane through the reference particle centroid as function of bulk concentration and Galileo number. The local mean concentration is normalized with the bulk concentration to highlight regions with higher (blue) and lower (red) than average concentration. The vectors show the PCA

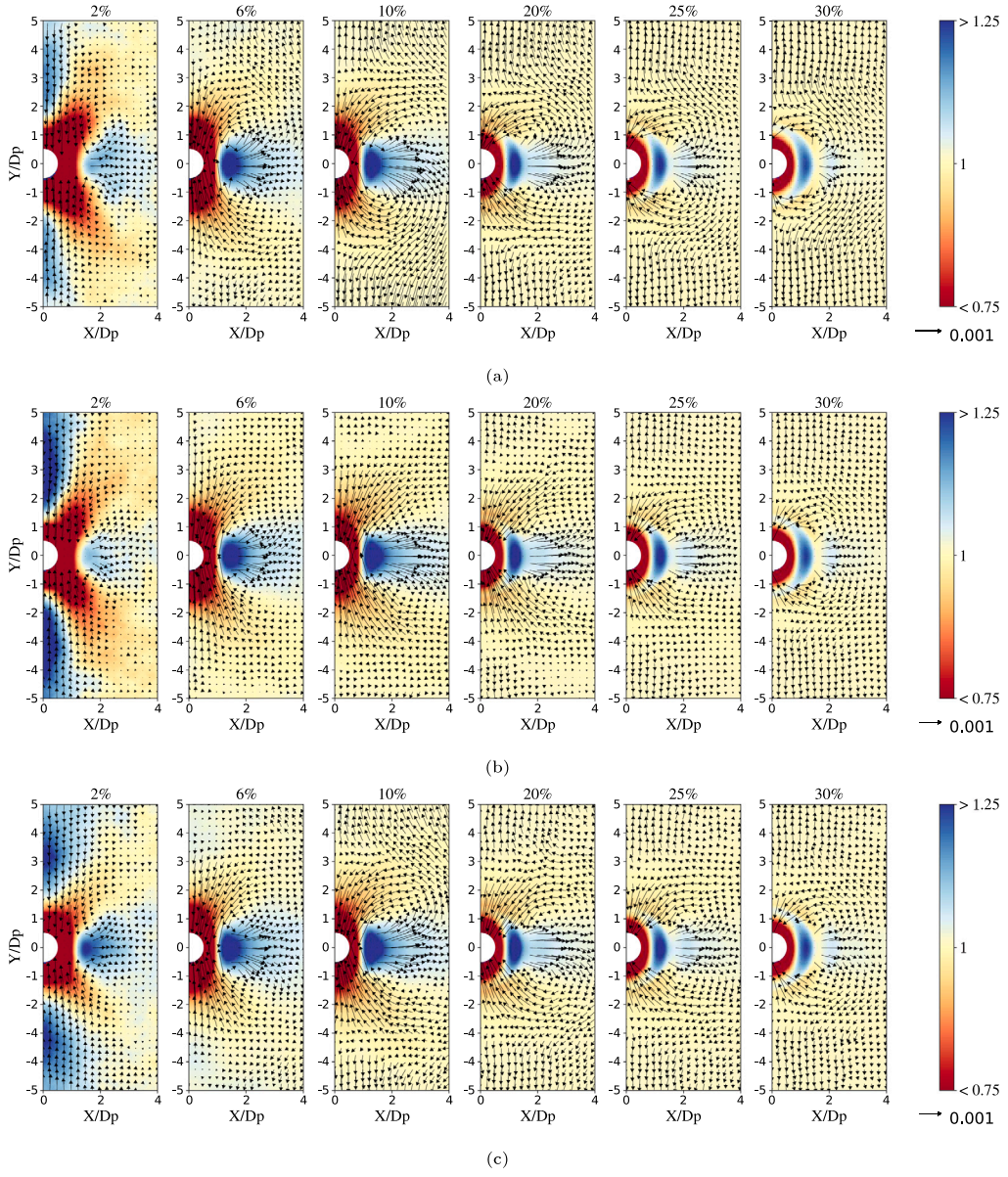

Fig. 3. Particle-conditioned average concentration field in the vertical plane through the reference particle centroid and normalized with the bulk concentration, $\overline{\gamma}/\phi$. The vectors represent the PCA relative particle velocity field. For clarity, the vectors within a radial distance of $1.5D_p$ of the reference particle centroid have been omitted as they are much larger than the vectors further away from the reference particle. The reference vector below the color legend has a magnitude of $0.001\sqrt{gD_p}$. Because of mirror symmetry only $x/D_p \geq 0$ is shown. The concentration is increasing from left to right from $\phi = 2$–30%. (a) $Ga = 144$, (b) $Ga = 178$, (c) $Ga = 210$.

relative particle velocity field. At first sight, the PCA concentration field does not vary much with the Galileo number and depends predominantly on the bulk concentration. At $\phi = 2\%$, we observe a clear tendency for vertical aggregation of particles. This is most pronounced at $Ga = 178$ and extends from $y/D_p \simeq 1.5 - 5$. At all three Galileo numbers, this is accompanied by an elevated concentration in the lateral direction around a spot centered at $x/D_p \simeq 1.5$ and fading away for larger x. At $\phi = 2\%$ particles thus show an enhanced likelihood to settle in vertical trains of several particle diameters long as well as in a pairwise side-by-side motion. The relative particle velocity field shows the tendency of vertically aligned particles to move towards the reference particle, consistent with the wake-trapping mechanism. At close encounter with the reference particle, a DKT-type instability seems to be responsible for a quick reconfiguration of vertically aligned particles towards horizontal side-by-side motion, consistent with the local pattern in the relative particle velocity and a characteristic X-shaped region near the reference particle with a lower than average concentration.

Interestingly, not shown here but discussed in Shajahan and Breugem (2020), the tendency of particles to aggregate in the vertical is even much more pronounced for $\phi = 0.5\%$ and $Ga = 144$, where the particle clusters are alike the columnar structures reported by Uhlmann and Doychev (2014) for $\phi = 0.5\%$ and $Ga = 178$. Contrary to $\phi = 2\%$, this is accompanied by a significantly less likelihood for particles to settle side-by-side (see Fig. 5a in Shajahan and Breugem (2020)). We observe from Fig. 3 that the tendency to aggregate in the vertical quickly vanishes with increasing bulk concentration. Already at $\phi = 6\%$ the tendency has almost completely disappeared, while simultaneously the tendency for pairwise side-by-side motion has become stronger as compared to $\phi = 2\%$. Thus, $\phi = 2\%$ marks the transition from the dilute to the moderate concentration regime, with a tendency of

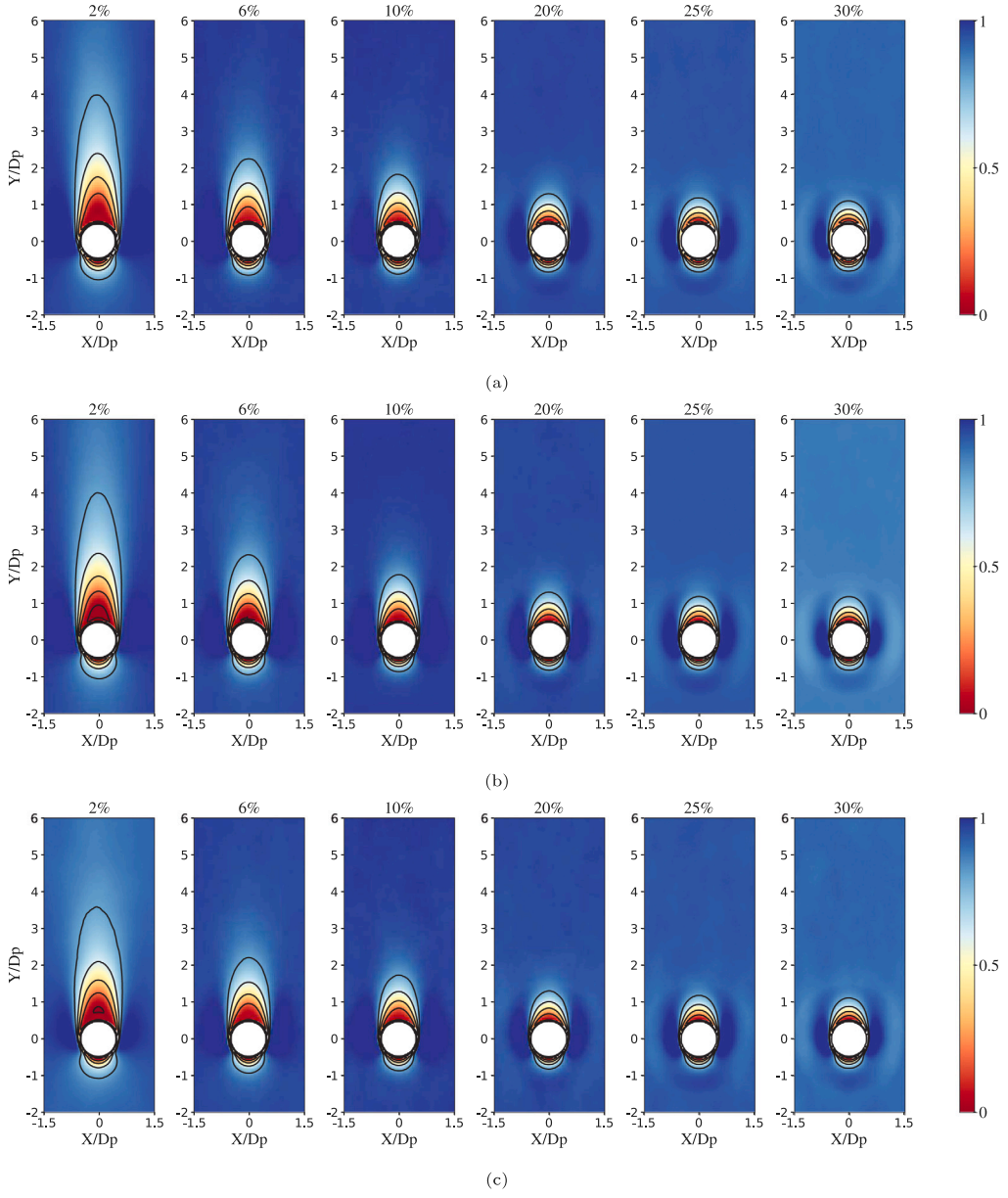

Fig. 4. Particle-conditioned average fluid flow field in the vertical plane through the reference particle centroid and normalized with the mean relative fluid velocity, $V_r = V_s - V_f$. The solid lines are isocontours varying from 0 to 0.8 at intervals of 0.2. Because of mirror symmetry only $x/D_p \geq 0$ is shown. The concentration is increasing from left to right from ϕ = 2–30%. (a) $Ga = 144$, (b) $Ga = 178$, (c) $Ga = 210$.

particles to aggregate in the vertical at lower bulk concentrations by the wake-trapping mechanism and a tendency of particles to settle side-by-side in a pairwise manner at a distance of $\sim 1.5D_p$ by a DKT-type instability at moderate bulk concentrations. The breakdown of the vertical aggregates in the moderate concentration regime might be related to the increased importance of short-range particle–particle interactions at the cost of long-range hydrodynamic interactions like wake trapping. This is consistent with a more localized preferential concentration pattern and a more confined particle recirculation pattern at higher ϕ. Recall that preferential settling in a dominant pairwise side-by-side configuration was reported before by Yin and Koch (2007) for the moderate Reynolds number regime ($Re_T = 10$, $\rho_p/\rho_f = 2$) at $\phi = 1\%$ and 5% with interparticle distances of $\sim 2.5D_p$ and $\sim 2D_p$, respectively. Thus, our results show that such dominant pairwise particle configuration is still present at similar bulk concentrations but more than tenfold higher Re_T.

From $\phi = 10$ to 20% we observe yet another transition from preferential setting in a pairwise side-by-side motion at moderate bulk concentrations ($2\% \lesssim \phi \lesssim 10\%$) towards a more and more concentric ring-like distribution in the dense regime ($\phi \gtrsim 10\%$). This indicates a tendency towards a random "hard-sphere distribution" consistent with the observations of Yin and Koch (2007) for $\phi = 20\%$ in the low and moderate Reynolds number regimes ($Re_T = 1$ and 10). They attributed the randomness of the distribution to chaotic motions from many-particle interactions. The layering in concentric rings originates from the restriction that hard spheres cannot overlap ('excluded volume effect') (Guazzelli and Morris, 2012). This causes a quasi-ordering of the distribution close to the reference particle, which quickly fades away over a distance of a few particle diameters related to increasingly uncorrelated motions of the spheres. We remark that at $\phi = 30\%$ the ring-like distribution is still not fully spherically symmetric, with a higher preference for horizontal than vertical particle alignment within the spherical shells, consistent with the local particle recirculation pattern. This suggests that weak DKT-type instabilities still play a role here.

Fig. 4 presents the results for the PCA relative vertical fluid velocity as function of bulk concentration and Galileo number. The relative velocity is scaled with the difference between the mean fluid and mean sedimentation velocity, $V_r = V_f - V_s = -V_s/(1-\phi)$ using that $\phi V_s + (1-\phi)V_f = 0$ for zero bulk mixture velocity. We loosely characterize the vertical extent of the fluid wake by the 0.8 isocontour of the normalized relative velocity (i.e., the upper contour in the plots). At $\phi = 2\%$, the vertical wake extent is then approximately $3.5D_p$ for $Ga = 144$ and $Ga = 178$ and around $3D_p$ for $Ga = 210$. Interestingly, the tip of the 0.8 isocontour roughly matches with the local concentration maximum in the vertical clusters observed in Fig. 3. Furthermore, although the effect of Ga appears to be fairly small, the larger wake extent for $Ga = 144$ and $Ga = 178$ seems consistent with the observation from Fig. 3 that vertical clustering is more confined in the lateral direction for $Ga = 144$ and $Ga = 178$ (stronger wake trapping due to a more pronounced fluid wake), while the particle surplus region around $x/D_p \simeq 1.5$ is most pronounced for $Ga = 210$ (stronger DKT-type instabilities).

The extent of the fluid wake declines rapidly when increasing the bulk concentration from the dilute to the moderately dense regime, in line with a weakening of the wake trapping mechanism and stronger local instability mechanisms such as DKT based on hydrodynamic interactions between neighboring particles. The decay of the wake extent continues when increasing the bulk concentration from the moderate to the dense regime, but at a much slower pace. Beyond $\phi \approx 10\%$, the extent of the wake is apparently so small that it can only facilitate weak DKT-type instabilities, while simultaneously short-range particle–particle interactions such as lubrication and collisions start to dominate the particle dynamics. At $\phi = 25\%$ and 30% the wake structure is nearly identical and limited in extent to about one particle diameter.

4.3. Mean particle sedimentation velocity

The mean particle sedimentation velocity was obtained by averaging the time series of the particle-mean velocity for $t > 50\sqrt{D_p/g}$ for which the flow was in a fully developed state. The result is shown in a log–log plot in Fig. 5 as function of the bulk void fraction, $1-\phi$, and Galileo number. The figure clearly shows the effect of hindered settling: the sedimentation velocity drops rapidly with decreasing bulk void fraction and hence increasing bulk concentration. For each Ga and $\phi \gtrsim 10\%$, the data points lie approximately on a straight line, in agreement with the Richardson–Zaki power-law relation given by Eq. (1). The dashed lines show the fit of Eq. (1) to the DNS data for $\phi \geq 10\%$. The values for the correction factor, k, and the power-law exponent, n, are given in Table 4 along with the values for n estimated from the following correlations provided by Richardson and Zaki (1954):

$$n = \begin{cases} \left[4.45 + 18\frac{D_p}{D_{pipe}}\right] \cdot (kRe_T)^{-0.1} & , \quad 1 < kRe_T < 200\,, \\ 4.45 \cdot (kRe_T)^{-0.1} & , \quad 200 < kRe_T < 500\,, \end{cases} \tag{5}$$

where D_p/D_{pipe} is the particle-to-pipe diameter ratio in the experiments of Richardson and Zaki. As the flow domain in the DNS is a rectangular box with triply periodic boundary conditions, we evaluated Eq. (5) both for $D_p/D_{pipe} = 0$ and $D_p/D_{pipe} = 1/25$ based on the lateral extent of the flow domain of $25D_p$. The actual confinement effect from the finite lateral domain extent in the DNS is expected to be in between these two extreme cases. Indeed, this appears to be the case for $Ga = 144$ and 178, see Table 4. For $Ga = 210$, the Richardson–Zaki correlation predicts no confinement effect on the sedimentation velocity. The corresponding DNS value for n is in fairly good agreement with the correlation estimate (deviation of +14%). Note that the DNS values for n are varying in a non-monotonic manner with Ga. Nonetheless, in all cases the value is close to 3, which indicates a nearly Ga-independent exponent over the currently investigated Ga range.

From Fig. 5 it can be observed that the Richardson–Zaki relation underestimates the sedimentation velocity for $\phi < 10\%$. The deviation

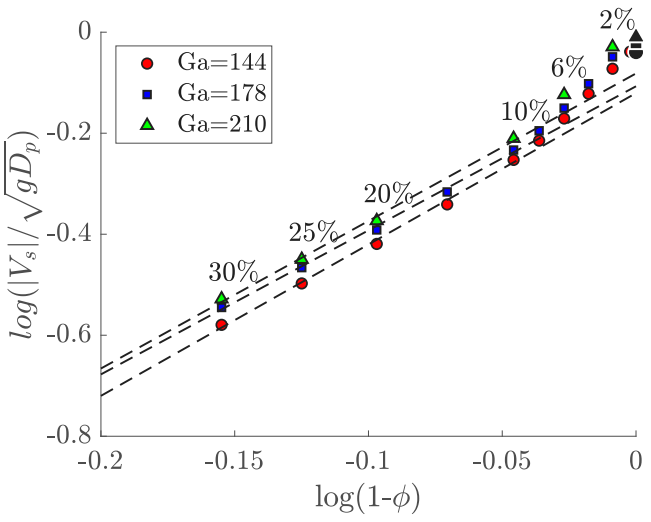

Fig. 5. Double-log plot of the normalized mean particle sedimentation velocity, $|V_s|/\sqrt{gD_p}$, as function of bulk void fraction, $1-\phi$, and Galileo number. The dashed lines represent fits of the Richardson–Zaki relation, Eq. (1), to the data points for $\phi \geq 10\%$. The black symbols at $\phi = 0$ indicate the mean single-particle terminal settling velocity, see Table 3.

increases for smaller ϕ and is largest for $\phi = 0$. Indeed, the fitted value for the correction factor k is significantly smaller than one. This is well known from literature, see, e.g., Felice (1999) and Yin and Koch (2007). Their reported values for k are in the range of 0.8–0.9, which is in good agreement with our DNS results. It is interesting to note that $\phi = 10\%$ marks the transition from the moderate concentration regime with an anisotropic microstructure towards the dense concentration regime with a more isotropic microstructure as discussed previously. Our results thus substantiate the suggestion of Yin and Koch (2007) that the Richardson–Zaki relation is associated with a "hard-sphere distribution". This also implies that the underestimation of the sedimentation velocity for $\phi < 10\%$ can be attributed to anisotropy of the microstructure, which in turn is originating from hydrodynamic particle interactions in the inertial regime (wake trapping and DKT-type instabilities). Finally, it is worth mentioning that for $Ga = 144$ and $\phi = 0.5\%$ the mean sedimentation velocity is very close to the mean single-particle settling velocity at the same Ga (difference of 0.2%). Thus we do not observe enhanced settling at this Ga, consistent with the presumed threshold of $Ga \approx 155$ for this.

4.4. Particle and fluid rms velocities

Fluctuations in the vertical particle velocity are defined as temporal deviations in the vertical particle velocity around the mean sedimentation velocity, $v_p' = v_p - V_s$. Similarly, vertical velocity fluctuations of the fluid phase are defined as $v_f' = v_f - V_f = v_f + \phi V_s/(1-\phi)$. As mean velocities in the horizontal directions are very close to zero, as expected for sedimenting suspensions, horizontal velocity fluctuations are simply defined by the instantaneous horizontal velocity. Figs. 6.a and 6.b depict the root-mean-square (rms) of the particle and fluid velocity fluctuations, respectively, both for the vertical (red symbols) and the lateral direction (blue symbols). Because of statistical symmetry, the horizontal rms velocities in x and z are nearly the same. Hence, they are represented by their average value, $\sqrt{(u_{p,rms}^2 + w_{p,rms}^2)/2}$.

Focusing on the particle rms velocities, a clear Ga-dependent peak can be observed in the vertical and to a lesser extent also the lateral direction in the range of $\phi = 4$–8%. The peak rms value varies in a non-monotonic fashion with Ga with the highest value for $Ga = 210$ and the lowest value for $Ga = 178$. On the other hand, when normalized with $\sqrt{gD_p}$, the particle rms velocities are nearly independent of Ga for

Table 4
Values for the correction factor, k, and the power-law exponent, n, in Eq. (1), obtained from fitting the DNS data for $\phi \geq 10\%$. The last two columns show estimates for n from the empirical Richardson–Zaki correlations given by Eq. (5).

Ga	k	n	n from Eq. (5) with $D_p/D_{pipe} = 0$	n from Eq. (5) with $D_p/D_{pipe} = 1/25$
144	0.83	3.00	2.69	3.12
178	0.82	2.85	2.62	3.05
210	0.85	2.92	2.57	2.57

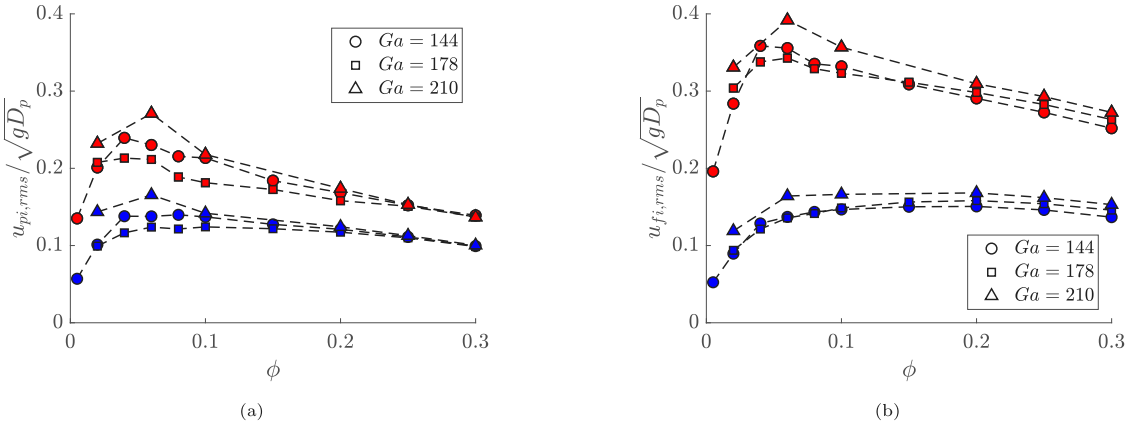

Fig. 6. Root-mean-square velocity of (a) particles and (b) fluid, normalized with $\sqrt{gD_p}$, and shown as function of ϕ and Ga. Red and blue symbols refer to the vertical (y) and lateral (x and z) direction, respectively. Circles, squares and triangles correspond to $Ga = 144$, 178 and 210, respectively. (For interpretation of the references to color in this figure legend, the reader is referred to the web version of this article.)

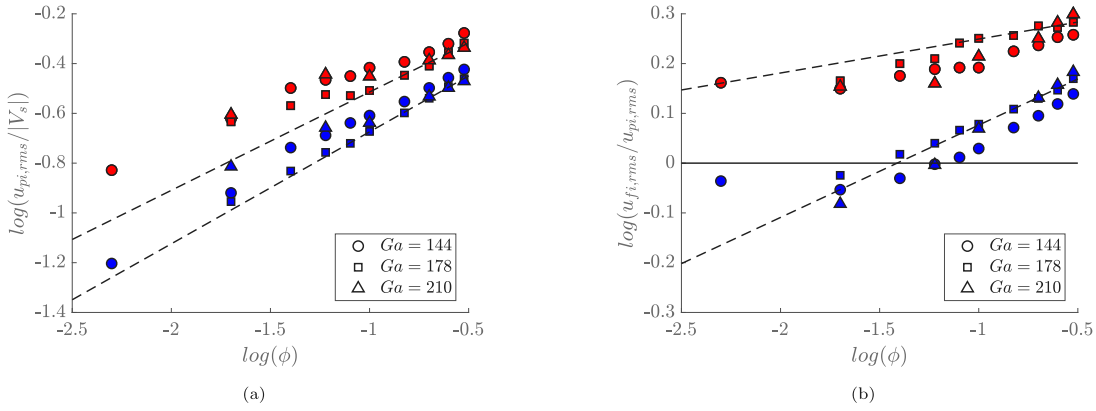

Fig. 7. Double-log plot of (a) the particle rms velocity normalized with $|V_s|$ and (b) the fluid/particle rms velocity ratio as function of ϕ and for the three different Galileo numbers. Red and blue symbols refer to the vertical (y) and lateral (x and z) direction, respectively. Circles, squares and triangles correspond to $Ga = 144$, 178 and 210, respectively. The dashed lines represent power-law fits of the DNS data to Eq. (6a) and (6b) for $Ga = 178$ and $\phi \geq 10\%$. (For interpretation of the references to color in this figure legend, the reader is referred to the web version of this article.)

$\phi \gtrsim 20\%$ and gradually decrease with increasing bulk concentration. The Ga-dependent peak in the particle rms velocity in the moderate concentration regime is consistent with contributions from hydrodynamic particle–particle interactions related to DKT-type instabilities. Conversely, the Ga-independent particle rms velocities in the dense concentration regime are consistent with short-range particle–particle interactions through lubrication and particle collisions. For the fluid velocity rms we observe a peak in the moderate concentration regime too, though less distinct for the lateral fluid rms having an almost constant value for $\phi \gtrsim 8\%$. Also, different from the particle rms velocities, the fluid rms velocities exhibit a mild Ga dependency over the entire concentration range.

In Fig. 7.a the particle rms velocities are plotted once again but now normalized with the mean sedimentation velocity and using logarithmic scales on both axes. Scaled in this manner, we observe that the particle rms velocities increase with increasing bulk concentration. In agreement with the DNS study of Zaidi (2018), for sufficiently high concentration the trend can be fairly well approximated by the following power-law relation:

$$\frac{u_{pi,rms}}{|V_s|} = C\phi^m, \tag{6a}$$

where the subscript i denotes the velocity component in direction i, and C and m are constants. We find that also the rms of the fluid velocity follows a power-law scaling, and so does the fluid-to-particle rms velocity ratio as is clear from Fig. 7.b:

$$\frac{u_{fi,rms}}{u_{pi,rms}} = \frac{C_{fi}}{C_{pi}}\phi^{(m_{fi}-m_{pi})}, \tag{6b}$$

where the subscripts p and f refer to the particles and fluid, respectively. We determined the power-law coefficients by fitting the DNS data to Eqs. (6a) and (6b) for $\phi \geq 10\%$. The fitted values are listed in Table 5.

Interestingly, our results contradict the findings from the DNS study of Zaidi (2018), who reported approximately equal power-law exponents for the vertical and the horizontal particle rms velocity: $m_{ph/v} = 0$ for $Re_T = 200$ and $m_{ph/v} = -0.1$ for $Re_T \gtrsim 300$. For our range of $Re_T =$

Table 5
Values for the coefficients in Eqs. (6a) and (6b) for, respectively, the normalized particle rms velocity and the fluid/particle rms velocity ratio, obtained from fitting the DNS data for $\phi \geq 10\%$. Subscripts p, f, v and h refer to, respectively, the particles, the fluid, the vertical and the lateral direction.

Ga	m_{pv}	C_{pv}	m_{ph}	C_{ph}	$m_{fv}-m_{pv}$	C_{fv}/C_{pv}	$m_{fh}-m_{ph}$	C_{fh}/C_{ph}
144	0.29	0.72	0.39	0.60	0.14	2.16	0.23	1.80
178	0.40	0.76	0.45	0.57	0.07	2.08	0.19	1.83
210	0.23	0.60	0.35	0.52	0.18	2.43	0.23	1.99

186–290, we consistently find $m_{ph} > m_{pv} > 0$ (i.e., different exponents and a rising trend) with m_{ph} and m_{pv} in the range of 0.35–0.45 and 0.23–0.40, respectively. The reason for our different findings is unclear, though it might be related to a different particle/fluid density ratio considered by Zaidi (2018) (2.5 vs 1.5 in our case).

Normalized with the mean sedimentation velocity, the lateral particle rms velocity rises steeper with bulk concentration than the vertical particle rms velocity. A higher vertical than horizontal rms particle velocity has been reported in many previous studies (Climent and Maxey, 2003; Yin and Koch, 2008; Uhlmann and Doychev, 2014; Zaidi et al., 2014; Hamid et al., 2014; Esteghamatian et al., 2017; Zaidi, 2018; Willen and Prosperetti, 2019). The anisotropy in the particle velocity fluctuations thus gradually decreases, though the power-law fits predict that it remains to exist in the very dense regime: assuming a maximum flowable packing fraction of $\phi \simeq 0.65$, the ratio of the vertical to the horizontal particle rms velocity approaches a value of approximately 1.2 for all three Galileo numbers. Finally, we observe from Fig. 7.b that the ratio of the fluid to the particle rms velocity is increasing with ϕ and generally larger than one. The only exception is the lower bulk concentration range ($\phi \lesssim 8\%$) for the lateral direction, where the fluid rms velocity is a bit smaller than the particle rms velocity.

4.5. Pdf of particle velocity

In Fig. 8 we show the normalized probability density function (pdf) of the particle velocity in the vertical (left) and the lateral (right) direction as function of bulk concentration and Galileo number (increasing from top to bottom). Note that $v_p - V_s < 0$ corresponds to particles falling faster than the mean sedimentation velocity as V_s is negative. For comparison, a Gaussian distribution is included in the plots. At first glance, the distribution of the particle velocities is close to Gaussian, in particular for $\phi > 6\%$, which agrees with the Gaussian distribution found for $\phi = 12\%$ in the simulations of Climent and Maxey (2003). Indeed, in the dense regime, the computed third and fourth standardized moment of the particle velocity, known as the skewness and kurtosis, are close to 0 and 3, respectively, as expected for a Gaussian distribution. The Ga-independent and Gaussian distribution at the higher bulk concentrations is consistent with a tendency towards a more random spatial arrangement of the particles and the dominant contribution of short-range particle–particle interactions to the particle dynamics. Furthermore, the collapse of the pdfs in the dense regime indicates that the velocity fluctuations scale with the rms velocity.

Although perhaps not immediately obvious from the pdfs, with increasing bulk concentration an increasing fraction of particles is instantaneously moving upwards. Using Eq. (6a), $v_p = 0$ corresponds to a standardized vertical velocity of $(v_p - V_s)/v_{p,rms} = (1/C_{pv})\phi^{-m_{pv}}$, which for $m_{pv} > 0$ indeed becomes smaller with increasing bulk concentration. For $Ga = 178$, we find that $v_p = 0$ corresponds to a standardized vertical velocity of 4.1 for $\phi = 6\%$, 2.5 for $\phi = 20\%$ and 2.1 for $\phi = 30\%$, which explains why at this Galileo number upward moving particles are hardly present for $\phi = 6\%$ but can be clearly observed for $\phi = 30\%$ in the snapshots of Fig. 2. The red dashed vertical line in Figs. 8.a,c,e marks the value of $-V_s/v_{p,rms}$ ($v_p = 0$) at $\phi = 30\%$. A few percent of all particles are moving upward at this concentration with the fraction decreasing with increasing Ga for the currently examined Ga range ($\sim 3\%$ at $Ga = 144$ vs less than 2% at $Ga = 210$).

Closer inspection for the lower concentration range reveals that the pdf of the vertical particle velocity is negatively skewed for $\phi = 0.5\%$ at $Ga = 144$ (Fig. 8(a)) and to a lesser extent also for $\phi = 2\%$ at $Ga = 178$ (Fig. 8(c)). The peak of the skewed pdf corresponds to particles falling a bit slower than the mean, while the longer left than right tail indicates that extreme events (say, $|v_p| > |V_s| + 2v_{p,rms}$) are more often associated with particles falling significantly faster than the mean. Skewed pdfs for the vertical particle velocity were also found in the previously mentioned sedimentation experiments by Huisman et al. (2016), though much more pronounced and associated with a significantly enhanced mean settling speed with respect to settling of a single particle in free space. Huisman et al. attributed the skewed pdf to the tendency of particles to form vertical columnar clusters, caused by the inertial trapping of particles in the wake of other particles underneath. The particles that fall in tandem are less exposed to the fluid flow and hence they settle faster than the other particles. The latter was clearly shown by Uhlmann and Doychev (2014) for the case of $Ga = 178$, $\rho_p/\rho_f = 1.5$ and $\phi = 0.5\%$.

Interestingly, we observe that the negatively skewed pdf for the vertical velocity corresponds to super-Gaussian behavior for the lateral velocity (a more peaky distribution with an enhanced kurtosis), which is most pronounced for $\phi = 0.5$–4% at $Ga = 144$ (Fig. 8(b)) and to a lesser extent for $\phi = 2\%$ at $Ga = 178$ (Fig. 8(d)). Similar behavior was reported by Fornari et al. (2016a) at $Ga \approx 145$, $\rho_p/\rho_f = 1.02$ and $\phi = 0.5$ and 1%. The higher peak around the origin is consistent with particles settling in rather stable vertical trains, whereas the longer tails might indicate strong horizontal particle excursions related to the initial formation or final breakup of the columnar structures. The skewed behavior of the vertical particle velocity and the super-Gaussian behavior for the lateral particle velocity both vanish with increasing bulk concentration. This is consistent with increasingly less stable columnar structures related to a smaller extent of the fluid wake (Fig. 4), disturbances from multi-particle interactions and more pronounced DKT-type instabilities in the moderate concentration range ($2\% \lesssim \phi \lesssim 10\%$).

4.6. Particle velocity correlations

Fig. 9 presents the temporal autocorrelations of the vertical (left) and lateral (right) particle velocity fluctuations as function of bulk concentration and Galileo number (increasing from top to bottom). For the vertical particle velocity, the autocorrelation is defined by:

$$\rho_{vv}(\tau) = \overline{v_p'(t)v_p'(t+\tau)}/\overline{v_p'^2}\,. \tag{7}$$

A first striking observation is the much slower decay of the autocorrelation of the vertical velocity fluctuations at $Ga = 144$ and $\phi = 0.5\%$ (Fig. 9(a)) as compared to the other autocorrelations of the vertical velocity at the same Ga but with higher bulk concentrations. The positive correlation at $\phi = 0.5\%$ up to $t = 400\sqrt{D_p/g}$ is consistent with the tendency of particles to settle preferentially in columnar structures. Also, a mild oscillatory behavior can be observed in this case with local minima near ~ 125 and $\sim 375\sqrt{D_p/g}$ and a local maximum in between at $\sim 225\sqrt{D_p/g}$, indicating an oscillation time period of $O(200-250)\sqrt{D_p/g}$. Interestingly, the autocorrelation of the corresponding lateral velocity fluctuations at $Ga = 144$ and $\phi = 0.5\%$ (Fig. 9(b)) gradually drops off to zero without signs of oscillatory behavior as seen for the vertical velocity component. Apparently, a

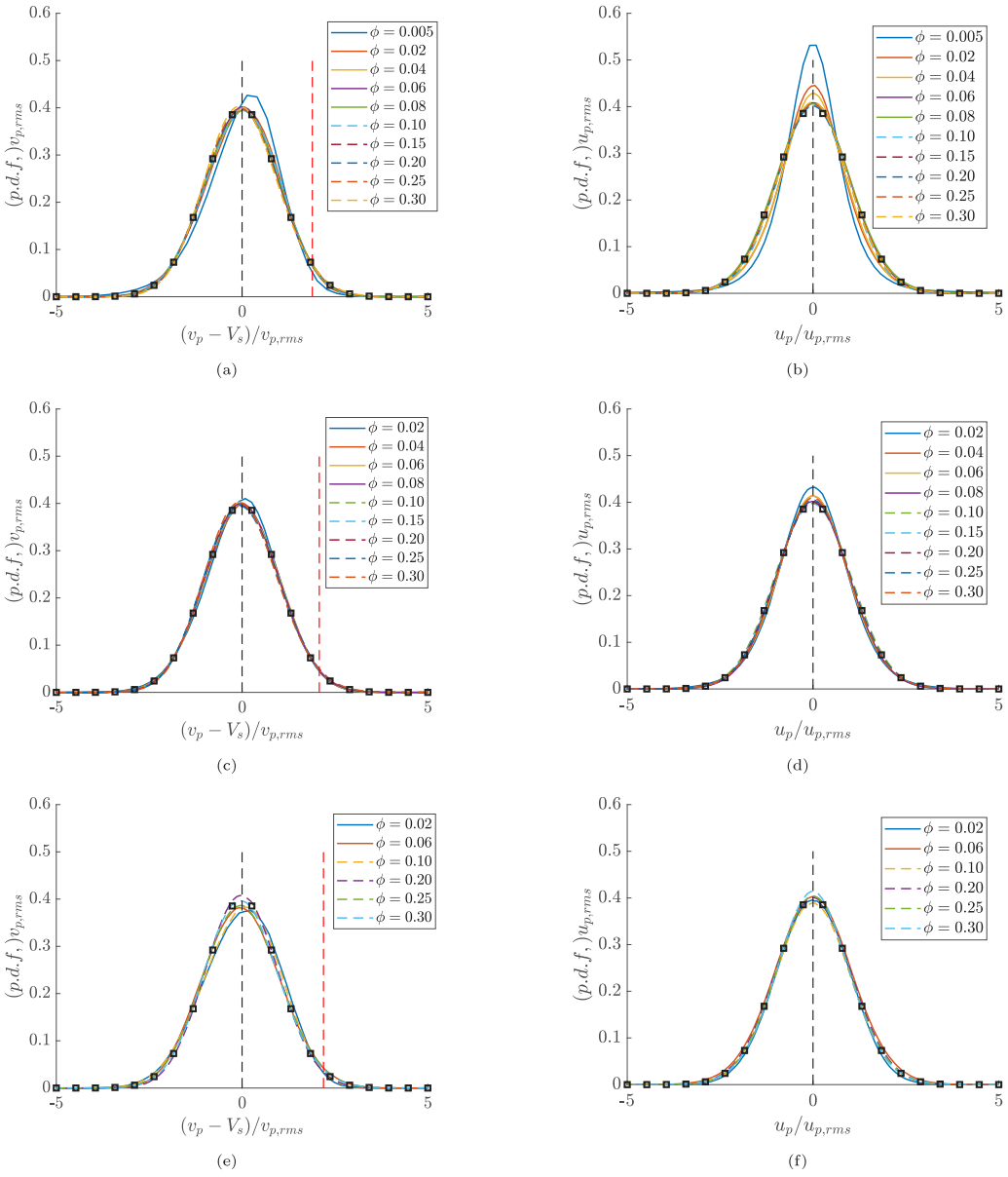

Fig. 8. Probability density function of the vertical (v_p, left) and lateral (u_p and w_p, right) particle velocity as function of bulk concentration and Galileo number (increasing from top to bottom). The pdf is normalized with the rms particle velocity. Black squares represent a Gaussian distribution. (a) Vertical velocity, $Ga = 144$, (b) lateral velocity, $Ga = 144$, (c) vertical velocity, $Ga = 178$, (d) lateral velocity, $Ga = 178$, (e) vertical velocity, $Ga = 210$, (f) lateral velocity, $Ga = 210$. The red dashed vertical line in (a), (c) and (e) marks the value of $-V_s/v_{p,rms}$ ($v_p = 0$) at $\phi = 30\%$. (For interpretation of the references to color in this figure legend, the reader is referred to the web version of this article.)

recurrent instability mechanism is at work that affects only the vertical and not the lateral velocity component at $\phi = 0.5\%$ and $Ga = 144$. This hints at the possible presence of kinematic waves, which travel in the vertical and may potentially disturb the earlier mentioned "stable" columnar structures present at this bulk concentration. We will discuss this in more detail later.

A second striking observation is the presence of a clear negative correlation peak for the vertical velocity component around $O(40-60)\sqrt{D_p/g}$ and subsequent oscillatory behavior for $\phi = 2$–20% at $Ga = 144$, $\phi = 4$–20% at $Ga = 178$, and $\phi = 6$–20% at $Ga = 210$. The oscillation frequency varies with bulk concentration and Ga, but is equal to $\sim 120\sqrt{D_p/g}$ at $\phi = 6\%$ for all Ga, thus roughly twice as low as the frequency found for $\phi = 0.5\%$ and $Ga = 144$. Interestingly, a similar oscillation period was found by Fornari et al. (2016a) for $Ga \approx 145$, $\rho_p/\rho_f = 1.02$ and $\phi = 1\%$, at least when the oscillation period is normalized with $\sqrt{D_p/[(\rho_p/\rho_f - 1)g]}$, i.e., using the reduced gravity instead of gravity. This suggests that the use of the reduced gravity is preferred over gravity when the density ratio is varied, as may also be expected from the gravity term in Eq. (3a).

For all three Galileo numbers, the negative peak and oscillatory behavior in the correlation for the vertical velocity are absent at $\phi = 25$ and 30%. This again is reminiscent of a change in the particle dynamics, now from the moderate to the dense regime, consistent with the transition to a "hard-sphere distribution" dominated by short-range particle–particle interactions for dense sedimenting suspensions. The observations for the correlation of the vertical velocity component in the moderate and dense regime hold also largely for the horizontal velocity component: a negative correlation peak and oscillatory behavior for the moderate concentrations and the absence of this for the most dense cases. A more quantitative frequency analysis will be discussed later when we present frequency spectra of the velocity fluctuations.

From the autocorrelations we have computed the integral time scale, τ_L, defined as:

$$\tau_L = \int_0^\infty \rho(\tau)\, d\tau\,. \tag{8}$$

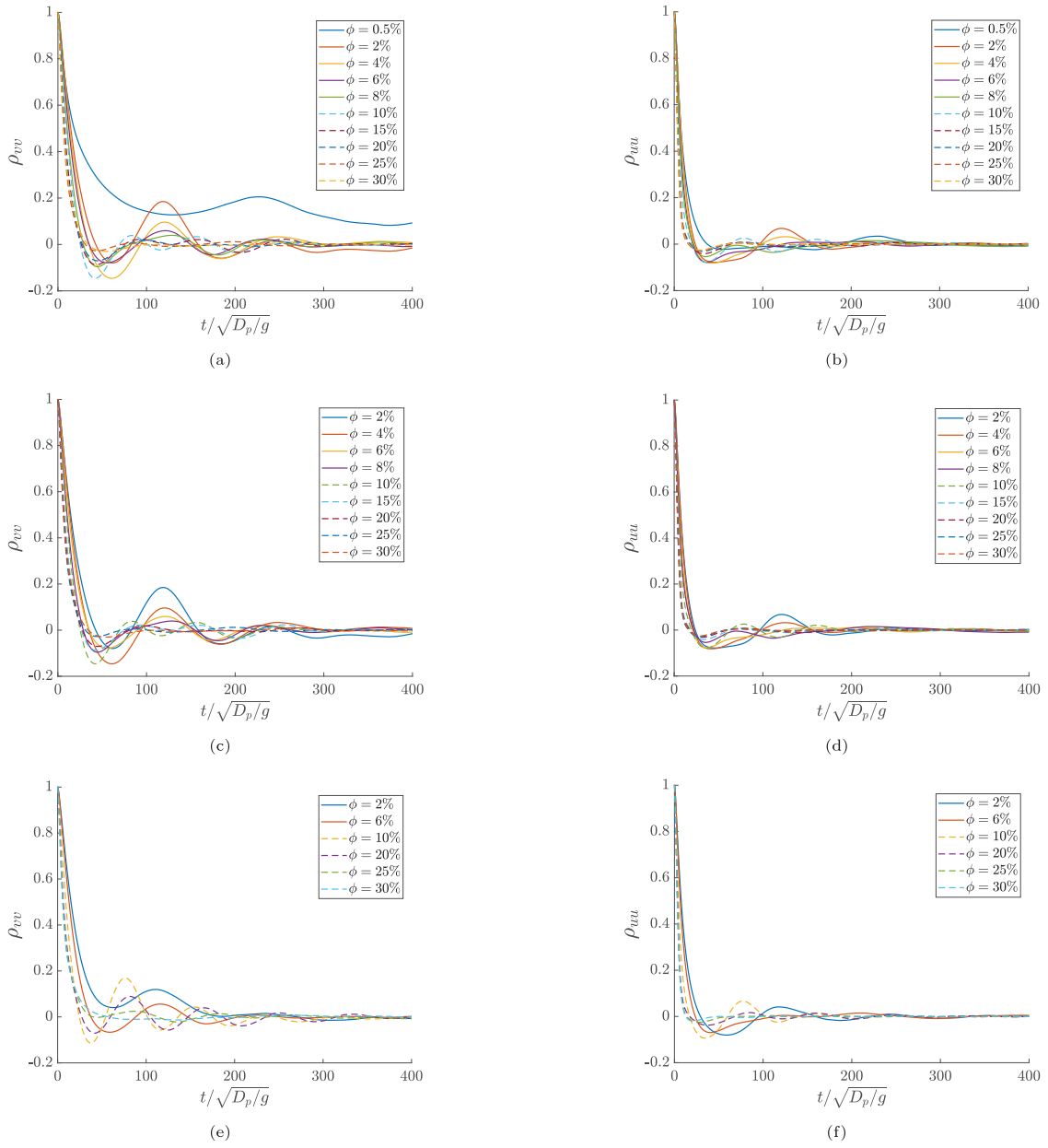

Fig. 9. Temporal autocorrelation of the vertical (v'_p, left) and lateral (u'_p and w'_p, right) particle velocity fluctuations, shown as function of bulk concentration and Galileo number (increasing from top to bottom). Because of statistical symmetry, the correlations are shown only for positive time shifts and, for clarity, only up to $400\sqrt{D_p/g}$. (a) Vertical velocity, $Ga = 144$, (b) lateral velocity, $Ga = 144$, (c) vertical velocity, $Ga = 178$, (d) lateral velocity, $Ga = 178$, (e) vertical velocity, $Ga = 210$, (f) lateral velocity, $Ga = 210$.

This is a rough proxy of the largest time over which particle velocity fluctuations are still correlated. In our previous study (Shajahan and Breugem, 2020) we multiplied it with the mean sedimentation velocity to estimate the corresponding vertical correlation distance. Fig. 10 shows $\tau_L/\sqrt{D_p/g}$ for the vertical (red) and lateral (blue) particle velocity fluctuations as function of ϕ and Ga. The normalized integral time scale rapidly drops off when increasing ϕ from the dilute to the moderate concentration regime, in particular for the vertical velocity, and then more gradually decreases towards a constant value of ~ 8 for the vertical and ~ 3 for the lateral velocity for $\phi > 10\%$. While the Galileo number has clearly some influence on τ_L in the dilute and moderate concentration regime, especially for the vertical velocity, it has almost no effect on τ_L in the dense regime. This is consistent with the importance of wake-related particle interactions for $\phi \lesssim 10\%$ and increasingly dominant short-range multi-particle interactions for $\phi \gtrsim 10\%$. The constant value of $\tau_L/\sqrt{D_p/g}$ in the dense regime implies that $\sqrt{D_p/g}$ is the relevant time scale for particle interactions in this regime, at least when the density ratio is kept constant as in our present study.

Instead of using Eq. (8), the integral time scale can also be obtained from an analysis of particle dispersion by means of the mean square particle displacement as function of time (Shajahan and Breugem, 2020). Twice the integral time scale marks the transition from the ballistic to the diffusive particle transport regime (Nieuwstadt et al., 2016). Furthermore, it can be shown that in the diffusive regime (i.e., for $t \gtrsim 2\tau_L$) the vertical particle diffusivity, $\mathcal{D}_{yy}$, is given by Nieuwstadt et al. (2016):

$$\frac{\mathcal{D}_{yy}}{\sqrt{gD_p^3}} = 2\left(\frac{v_{p,rms}}{\sqrt{gD_p}}\right)^2\left(\frac{\tau_{L,vv}}{\sqrt{D_p/g}}\right). \tag{9}$$

A similar expression can be derived for the horizontal particle diffusivity. The diffusivity is higher in the vertical than in the horizontal direction, related to the higher rms velocity and integral time scale in

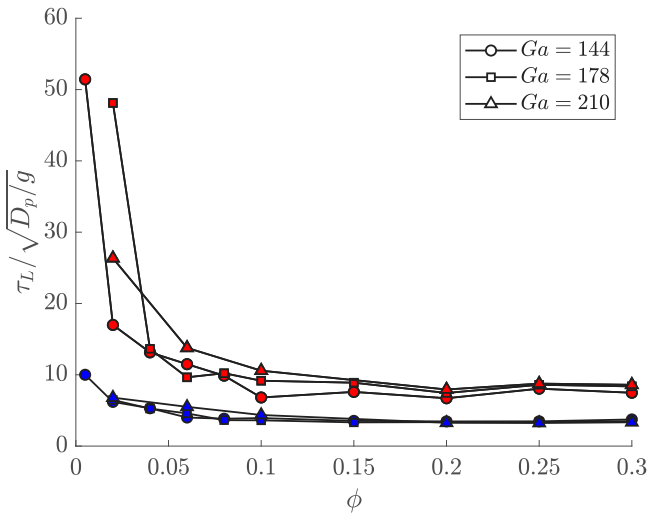

Fig. 10. Normalized integral time scale $\tau_L/\sqrt{D_p/g}$ for the vertical (v_p', red) and lateral (u_p' and w_p', blue) particle velocity fluctuations as function of ϕ and Ga. (For interpretation of the references to color in this figure legend, the reader is referred to the web version of this article.)

the vertical. It is also higher for the dilute and moderate concentration regime than for the dense regime. As the normalized rms velocity and the normalized integral time scale are both independent of Ga in the dense regime, so does also the particle diffusivity: it scales with $\sqrt{gD_p^3}$ and gradually decreases with concentration in the dense regime.

For DKT-type instabilities it may be expected that vertical and horizontal velocity fluctuations are related to each other. To investigate this, we have computed the cross-correlation defined by:

$$\rho_{vu}(\tau) = \frac{\overline{v_p'(t)u_{ph}'(t+\tau)}}{\overline{v_p'u_{ph}'}} \quad \text{with} \quad u_{ph} = \sqrt{u_p^2 + w_p^2}. \tag{10}$$

The cross-correlation is shown in Figs. 11.a–c as function of bulk concentration and Galileo number. For bulk concentrations of up to 10%, we observe a positive correlation peak larger than 1 at a slightly negative time lag followed by a strong anti-correlation peak for a positive time lag of $\tau/\sqrt{D_p/g} \approx 10$–16. The anticorrelation peak is even larger than the positive correlation peak for $\phi = 0.5$ and 6% at $Ga = 144$ and for $\phi = 6$ and 10% at $Ga = 210$. We attribute this behavior to DKT-type events in which a particle gets trapped in the wake of another particle and will display a more vertical path ("drafting" with faster settling and hence $v_p' < 0$, and $u_{ph}' < 0$), while directly after close contact with the leading particle ("kissing"), it will experience a strong perturbation in its horizontal velocity at a still enhanced fall velocity ("tumbling" with $u_{ph}' > 0$ and $v_p' < 0$). This also explains why the anti-correlation peak vanishes in the dense regime where short-range multi-particle interactions and collisions dominate the particle dynamics. The chaotic motions in the dense regime are responsible for a more symmetric cross-correlation, which rapidly drops off to zero for non-zero time lag. As seen before for the autocorrelations, also the cross-correlation exhibits oscillatory behavior for the lower concentration range, which in some cases is most pronounced for positive time lags (e.g., for $\phi = 2\%$ at $Ga = 144$ and 178 with an oscillation period of $O(100)$ time units, and for $\phi = 10\%$ at $Ga = 144$ and $Ga = 210$ with an oscillation period of $O(65)$ time units). We speculate that in these cases DKT-type instabilities might be responsible for the onset of large-scale instabilities such as kinematic waves. Conversely, the presence of slow oscillations for negative time lags, such as for $\phi = 6\%$ at all Ga, would then suggest that the opposite may also be true and that kinematic waves may trigger DKT-type instabilities by local compaction of the suspension along the vertically traveling waves. We will explore this in more detail later.

To assess the coupling of the vertical with the horizontal particle velocity fluctuations, we computed the corresponding zero-lag cross-correlation coefficient from:

$$r_{vu} = \frac{\overline{v_p'u_{ph}'}}{v_{p,rms}u_{ph,rms}}. \tag{11}$$

The cross-correlation coefficient is equal to ± 1 when the vertical and horizontal particle velocity fluctuations would be instantaneously fully coupled and is equal to 0 when they are completely uncorrelated with each other. The results are depicted in Fig. 11(d) as function of ϕ and Ga. The coupling of the velocity fluctuations is clearly strongest for $\phi = 2$ and 4%, where DKT-type instabilities are active. In the moderate concentration regime, it is highest for $Ga = 178$, except for $\phi = 2\%$ where a slightly higher peak is found for $Ga = 144$. For all bulk concentrations and Galileo numbers, the coupling is smaller than 0.16 and thus seems relatively weak. This might indicate that chaotic particle interactions are interfering with DKT-type instabilities already in the moderate concentration regime. It is striking that at $Ga = 144$ the correlation coefficient is about a factor 1.5 smaller for $\phi = 0.5\%$ than for $\phi = 2\%$. However, note that the correlation coefficient is based on the covariance at zero time lag, while for $\phi = 0.5\%$ the anti-correlation peak corresponds to a lagged cross-correlation of about -1.7. The corresponding lagged correlation coefficient is thus about $-1.7 \times 0.104 \approx -0.18$. Similarly, at $\phi = 2\%$ the cross-correlation peaks around 1.15 at a slightly negative time shift, with a corresponding lagged correlation coefficient of about $1.15 \times 0.155 \approx 0.18$. Thus, the lagged correlation coefficients at $\phi = 0.5$ and 2% are comparable in magnitude.

4.7. Frequency spectra of particle velocities

To investigate the presence of dominant frequencies in the particle velocity fluctuations, we have computed the frequency spectrum of the particle velocity from the Fourier transform of the temporal autocorrelation. For the vertical velocity component this is given by:

$$\frac{E_{vv}(\omega)}{R_{vv}(0)\sqrt{D_p/g}} = 2\,\Re\left(\frac{1}{2\pi}\int_{-\infty}^{\infty}\rho_{vv}(\tau)e^{-i\omega\tau}d\tau\sqrt{\frac{g}{D_p}}\right), \tag{12a}$$

where $\Re(..)$ denotes the real part of the transform and where we normalized the spectrum with the velocity variance ($R_{vv}(0) = \overline{v_p'^2}$) and the gravitational time ($\sqrt{D_p/g}$). Note that $\rho_{vv}(-\tau) = \rho_{vv}(\tau)$ at statistically steady state and this is how we obtained the autocorrelation for negative time lags. The frequency spectrum describes the contribution of the different frequency components of the velocity signal to the overall velocity variance and hence the one-sided integral over the normalized spectrum is equal to 1:

$$\int_0^{\infty}\frac{E_{vv}(\omega_*)}{R_{vv}(0)\sqrt{D_p/g}}d\omega_* = 1, \tag{12b}$$

where $\omega_* = \omega\sqrt{D_p/g}$. Also, the value of the frequency spectrum at zero frequency is related to the integral time scale defined by Eq. (8) according to:

$$\frac{E_{vv}(0)}{R_{vv}(0)\sqrt{D_p/g}} = \frac{2}{\pi}\frac{\tau_{L,vv}}{\sqrt{D_p/g}}. \tag{12c}$$

Fig. 12 presents the normalized frequency spectra for the vertical (left) and horizontal (right) particle velocity fluctuations as function of bulk concentration and Galileo number (increasing from top to bottom). At all Galileo numbers, clear peak frequencies can be observed in the lower frequency range for $\phi \lesssim 10\%$, while no distinct peaks at all are present at $\phi = 25$ and 30%. This suggests that the frequency peaks for the lower concentration range can be attributed to wake-related hydrodynamic particle interactions. Focusing on $Ga = 144$, for $\phi = 0.5$ and 2% very low peak frequencies with $\omega_* < 0.01$ are present in the vertical velocity spectrum, which are likely related to

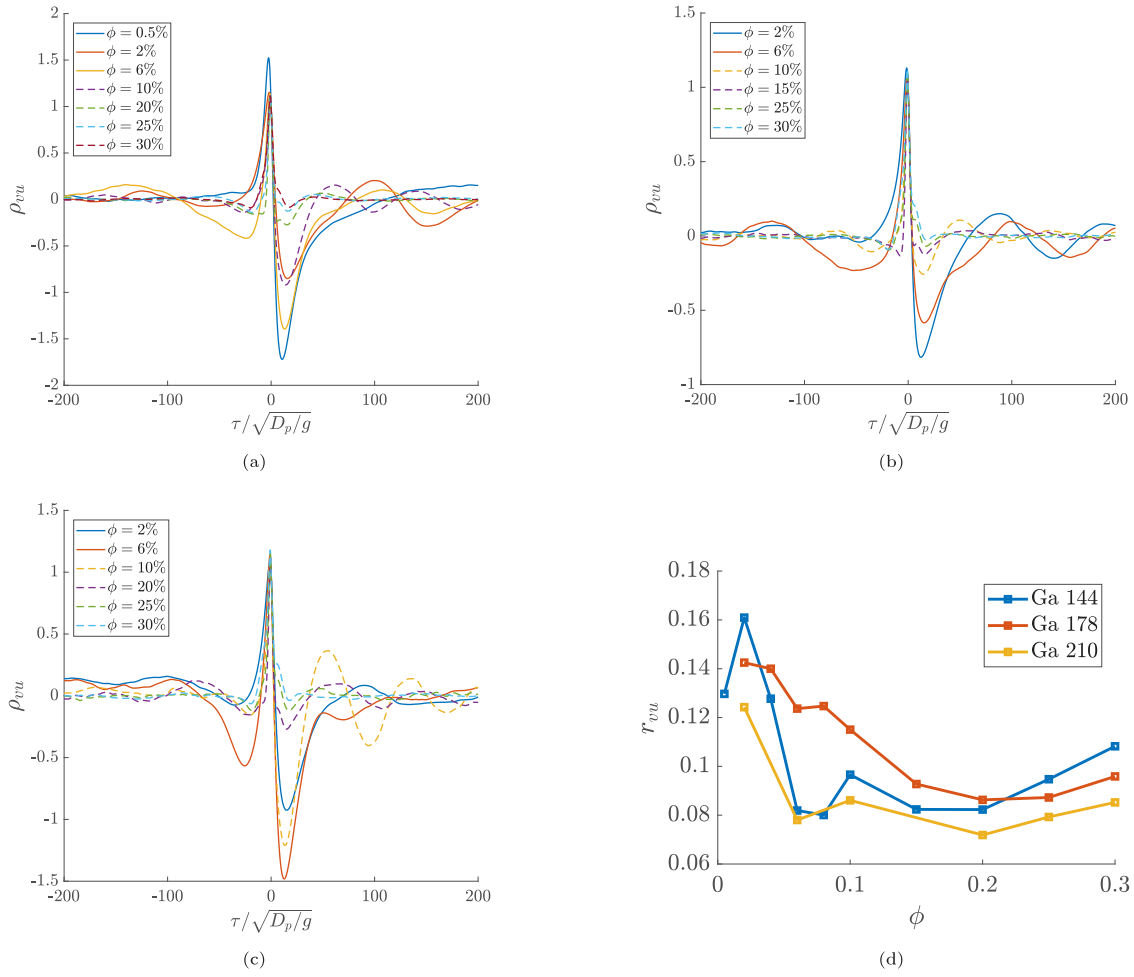

Fig. 11. Temporal cross-correlation of vertical velocity fluctuations with fluctuations in the horizontal velocity magnitude, shown as function of bulk concentration and Galileo number. For clarity, only a range of 400 time units is shown, centered around 0. (a) $Ga = 144$, (b) $Ga = 178$, (c) $Ga = 210$. (d) Correlation coefficient for fluctuations in the vertical velocity and in the magnitude of the horizontal velocity, shown as function of bulk concentration and Galileo number.

the presence of persistent columnar structures in which particles settle at an enhanced velocity in these cases, especially for $\phi = 0.5\%$. For $\phi = 2$–8%, where DKT-type instabilities are active, a clear peak is found in both the horizontal and the vertical velocity spectrum at $\omega_* \approx 0.05$ with a corresponding oscillation period of $\approx 126\sqrt{D_p/g}$. This agrees well with the oscillation period of $\sim 120\sqrt{D_p/g}$ observed earlier in the autocorrelation for the vertical particle velocity at $\phi = 6\%$ for all Ga. For $\phi = 10\%$, a dominant peak frequency is present at $\omega_* \approx 0.08$ in both spectra with a corresponding oscillation period of $\approx 79\sqrt{D_p/g}$. Upon further increasing the bulk concentration beyond 15%, no dominant peak frequencies can be observed anymore and the spectrum varies more gradually with frequency. The spectra for $Ga = 178$ and 210 are qualitatively similar to the spectra for $Ga = 144$. The same peak frequencies can be observed, though the height of the peaks depends on Ga. For $Ga = 210$ we also observe a significant frequency peak at $\omega_* \approx 0.08$ for $\phi = 20\%$.

Interestingly, for $\phi \gtrsim 20\%$, both the normalized horizontal and the normalized vertical velocity spectra collapse for $\omega_* \lesssim 0.02$ and $\omega_* \gtrsim 0.1$, independent of the Galileo number. For $\omega_* \lesssim 0.02$ the spectra are constant and approximately equal to 5 for the vertical velocity and 2 for the horizontal velocity. This is consistent with the values of approximately 8 and 3 for the normalized integral time scale of, respectively, the vertical and the horizontal velocity in the dense regime, see Fig. 10 and Eq. (12c). For $\omega_* \gtrsim 0.1$, the vertical velocity spectrum varies with the frequency as ${\omega_*}^{-1.25}$ between $0.1 \lesssim \omega_* \lesssim 0.4$ and as ${\omega_*}^{-2.75}$ for $\omega_* \gtrsim 0.4$. For the same frequency range, the horizontal velocity spectrum scales as ${\omega_*}^{-0.6}$ between $0.1 \lesssim \omega_* \lesssim 0.4$ and as ${\omega_*}^{-3}$ for $\omega_* \gtrsim 0.4$. Our results are consistent with an approximate $-10/3$ slope of the vertical particle velocity spectrum at high frequencies for $Ga = 4.6$–153.6 in Yao et al. (2021), though no explanation was provided by them for the observed scaling.

The Ga-independent scaling of the velocity spectra in the dense regime suggests that the particle dynamics is dominated by multi-particle interactions by viscous lubrication and possibly particle collisions. Furthermore, the collapse of the spectra for the low and the higher frequency range indicates that in the dense regime the rms particle velocity and $\sqrt{D_p/g}$ are the characteristic velocity and the characteristic time scale of the particle velocity fluctuations. In fact, this is in line with the Gaussian distribution of the normalized particle velocity and the constant $\tau_L/\sqrt{D_p/g}$ in the dense regime, irrespective of the value of the Galileo number. The change in the power-law scaling exponent at $\omega_* \approx 0.4$, corresponding to an oscillation period of approximately $16\sqrt{D_p/g}$, indicates a change in the underlying dynamics. It is also striking that for $0.1 \lesssim \omega_* \lesssim 0.4$ the power-law scaling exponent for the horizontal velocity spectrum is approximately a factor 2 smaller than the power-law scaling exponent for the vertical velocity spectrum, while for $\omega_* \gtrsim 0.4$ the power-law scaling exponents are nearly the same. In Appendix A we propose a model that predicts an ${\omega_*}^{-3}$ scaling of the spectra for $\omega_* \gtrsim 0.4$. It is based on the inertial response of the particles to small-scale flow structures with a presumed k^{-3} wavenumber spectrum, as has been also observed for homogeneous bubble swarms (Lance and Bataille, 1991; Risso, 2018), that are advected by the mean relative fluid flow towards the particles and effectively impose high-frequency force perturbations on the particles.

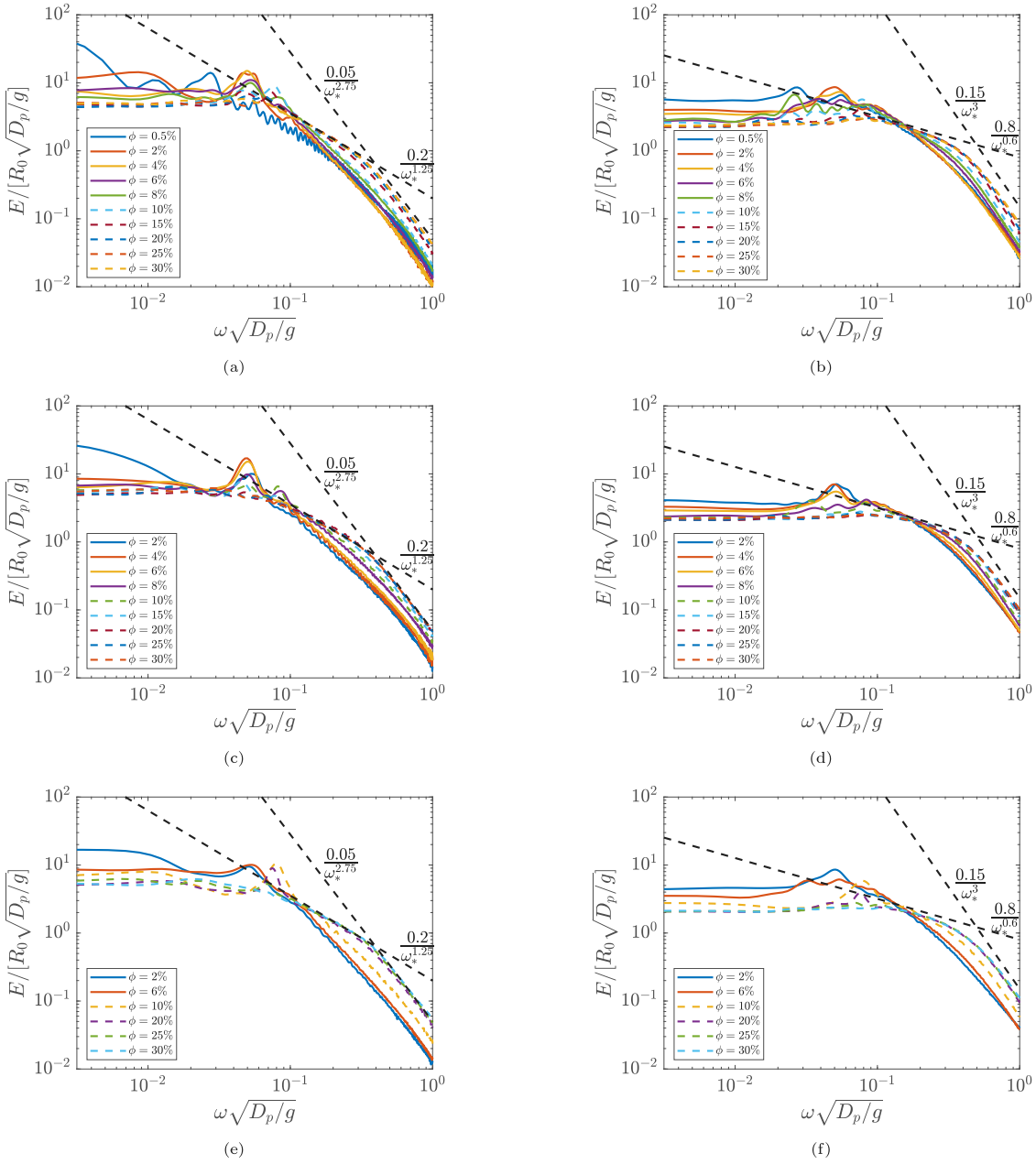

Fig. 12. Double-log plots of the normalized frequency spectra of the vertical (v_p', left) and horizontal (u_p' and w_p', right) particle velocity fluctuations, shown as function of bulk concentration and Galileo number (increasing from top to bottom). Black dashed lines indicate power-law scaling of the normalized spectra in the normalized frequency for the most dense concentration cases in specific frequency ranges. (a) Vertical velocity, $Ga = 144$, (b) horizontal velocity, $Ga = 144$, (c) vertical velocity, $Ga = 178$, (d) horizontal velocity, $Ga = 178$, (e) vertical velocity, $Ga = 210$, (f) horizontal velocity, $Ga = 210$.

We also discuss the scaling behavior of the spectra for $0.1 \lesssim \omega_* \lesssim 0.4$. It is left for future research to investigate the physical origin of the power-law scalings in more detail and to what extent it can be generalized to other Galileo numbers and density ratios.

4.8. Role of particle collisions

From Eq. (3a) it follows that at statistically steady state the mean vertical hydrodynamic drag force ($\overline{F}_d$) should balance the net gravity force (F_{ng}) acting on the particles:

$$\frac{\overline{F}_d}{\rho_f g D_p^3} = -\frac{\overline{F}_{ng}}{\rho_f g D_p^3} = \frac{\pi}{6}\left(\frac{\rho_p}{\rho_f} - 1\right)(1-\phi), \tag{13}$$

where the net gravity force is the downward gravity force minus the upward and concentration-dependent Archimedes force related to the upward hydrostatic pressure gradient. Note that the mean collision force acting on the particles is zero as during a collision between two particles the same collision force acts on both particles but in opposite direction and hence their sum is zero. To assess the importance of particle collisions we have therefore evaluated the mean magnitude of the collision force, $|\overline{\mathbf{F}_c}| = \sqrt{\overline{F_{c,x}^2} + \overline{F_{c,y}^2} + \overline{F_{c,z}^2}}$. In Fig. 13(a) we show the mean vertical hydrodynamic drag force and the mean magnitude of the collision force as function of ϕ and Ga. The forces have been normalized with the net gravity force. From this figure we observe first that the normalized mean drag force is constant and equal to 1, which substantiates that the suspension is in a statistically steady state in all cases. Second, we observe that the effect of collision forces seems negligible for $\phi \lesssim 10\%$, in line with the dominant contribution of long-range hydrodynamic particle interactions to the overall particle dynamics (inertial wake suction and DKT-type instabilities). With increasing bulk

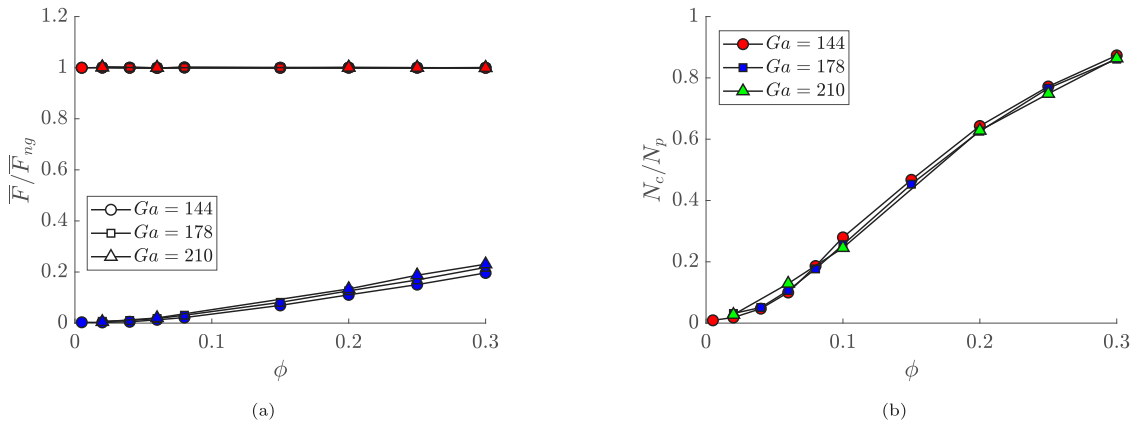

Fig. 13. (a) Mean vertical drag force ($\overline{F}_d$, red symbols) and mean magnitude of the collision force ($\overline{|\mathbf{F}_c|}$, blue symbols) normalized with the net gravity force ($\overline{F}_{ng}$) and shown as function of ϕ and Ga. Circles, squares and triangles correspond to $Ga = 144$, 178 and 210, respectively. (b) Average number of particles undergoing a collision during a computational time step (N_c), scaled with the total number of particles (N_p) and shown as function of ϕ and Ga.

concentration, collisions become gradually more important, though the mean magnitude of the collision force is still only about 20% of the net gravity force at the highest concentration. Third, we observe that the collision force is nearly independent of Ga, which might be related to the scaling with the net gravity force as this is ultimately the driving force responsible for sedimentation. Besides, in the dense regime, the relevant velocity and length scales are proportional to $\sqrt{gD_p}$ and D_p, respectively. Thus, when the collision force is scaled with gD_p^3 or, alternatively, with the net gravity force that is proportional to gD_p^3, it is expected that the collision force is independent of Ga, at least in the dense regime.

To further assess the influence of collisions on the particle dynamics, we have also computed the average number of colliding particles by counting at every time instant the number of particles with a non-zero collision force and averaging this number over time. The average number normalized with the total number of particles is shown in Fig. 13(b). We observe a gradual increase in the number of collisions as function of concentration, which is nearly independent of Ga. At the lowest concentration hardly any particle is colliding, at $\phi = 10\%$ this is about 25% of the total number of particles and at $\phi = 30\%$ this is nearly 90%. The high collision likelihood and the seemingly small mean magnitude of the collision force at $\phi = 30\%$ suggest that collisions are frequent but gentle in the dense regime. This is likely related to viscous lubrication between particles that tends to reduce the relative velocity between two approaching particles prior to their collision. This can be further assessed by means of the impact Stokes number, a measure of the initial relative momentum of the approaching particles to the typical loss of their relative momentum by viscous lubrication (Davis et al., 1986):

$$St = \frac{\rho_p \left(\frac{1}{6}\pi D_p^3\right) v_{rel}}{\frac{3}{2}\pi\rho_f \nu_f D_p^2}, \tag{14a}$$

where v_{rel} is the initial relative approach velocity. For $St \lesssim 10$ the particles will not rebound upon a collision due to strong viscous damping by lubrication, while $St \gtrsim 10^3$ corresponds to the granular regime where the particles will rebound with their initial approach velocity times the dry coefficient of restitution (Legendre et al., 2006). For simplicity, we restrict ourselves to collisions in the vertical as velocity fluctuations are strongest in this direction. We model the typical relative velocity between two particles by $v_{rel} = \sqrt{(v'_{p,1} - v'_{p,2})^2} \approx \sqrt{2}\, v_{p,rms}$ based on the crude assumption that in the dense regime the chaotic motions of the particles are uncorrelated. Using Eqs. (1) and (6a) we can then rewrite Eq. (14a) into the following form:

$$St = \frac{\sqrt{2}}{9} \cdot \frac{(\rho_p/\rho_f)\, Ga}{\sqrt{(\rho_p/\rho_f) - 1}} \cdot \frac{k|V_T|}{\sqrt{gD_p}} \cdot C_{pv}\phi^{m_{pv}}(1-\phi)^n, \tag{14b}$$

where the values of $|V_T|/\sqrt{gD_p}$, C_{pv} and m_{pv}, and n, are listed as function of Ga in Tables 3–5, respectively. Evaluating St for $\phi = 10\%$, we find that $St \approx 10$, 10 and 15 for $Ga = 144$, 178 and 210, respectively. Similarly, for $\phi = 30\%$, we find that $St \approx 6$, 8 and 9, respectively. The low values of St are supporting evidence that in the dense regime particle interactions are indeed dominated by viscous lubrication rather than actual particle collisions, at least for the currently investigated range of Ga and density ratio of 1.5. Based on a similar analysis, Willen and Prosperetti (2019) reached at the same conclusion for their simulations at $Ga = 49.7$–99.4 and $\rho_p/\rho_f = 2$–5.

The dominant contribution from viscous lubrication in the dense regime may also be understood from analyzing the Reynolds number based on the "mean collision distance", which we define as the typical distance traveled by two particles from the moment they start approaching each other till the moment that they collide. We estimate this distance by $\sqrt{2}\,\lambda_{\mathrm{mfp}}$, where λ_{mfp} is the "mean free path" traveled by a particle between two consecutive collisions (the collision distance is a factor $\sqrt{2}$ larger to account for the relative motion between particles). Based on kinetic theory of granular gases, see Eq. 13 in Willen and Prosperetti (2019), the mean free path is modeled as:

$$\lambda_{\mathrm{mfp}} = \frac{D_p}{6\sqrt{2}\phi} \cdot \frac{2(1-\phi)^3}{(2-\phi)}. \tag{15}$$

The associated Reynolds number based on the collision distance and relative particle velocity can now be estimated from:

$$Re_{col} = \frac{(\sqrt{2}\lambda_{\mathrm{mfp}})(\sqrt{2}v_{p,rms})}{\nu_f} = \frac{1.5}{(\rho_p/\rho_f)\phi} \cdot \frac{2(1-\phi)^3}{(2-\phi)} \cdot St. \tag{16}$$

For $\phi = 10\%$, $Re_{col} \approx 75$, 80 and 116, for $Ga = 144$, 178 and 210, respectively. Similarly, for $\phi = 30\%$, we find that $Re_{col} \approx 9$, 11 and 13, respectively. For $\phi = 10\%$, the collision Reynolds number is thus well within the inertial regime, which leaves room for inertial interactions before lubrication starts to become dominant at close distance between the approaching particles. For $\phi = 30\%$, the collision Reynolds number is already in the weakly inertial regime, and thus lubrication sets in much sooner after particles start approaching each other.

4.9. Kinematic waves

As mentioned in the introduction, sedimenting suspensions may exhibit kinematic waves. They manifest themselves as vertically propagating waves in the horizontal plane average concentration, defined by $\Phi(y,t) = \langle\gamma\rangle_h$, where $\gamma(x,y,z,t)$ is the solid phase indicator function (equal to 1 in the solids and 0 in the fluid) and the brackets denote the average over the horizontal directions. To visualize the presence of kinematic waves in the present simulations, in Fig. 14(a), 14(c) and

14(e) we have plotted the plane-averaged concentration normalized by the bulk concentration as function of height and time at $\phi = 30\%$ for each Galileo number.

At first sight, the space–time diagrams in Fig. 14 look rather noisy. Significant variations in the plane average concentration can be observed of $O(25\%)$ of the bulk concentration. Note that $\phi = 30\%$ corresponds to an average number of $0.3L_xL_z/(\pi D_p^2/8) \approx 477$ spheres passing through a horizontal plane in the computational domain, where $\pi D_p^2/8$ is the average area of the circle formed when randomly cutting a sphere in the horizontal. Thus, a variation of $\pm 25\%$ in the local concentration corresponds to variations of $O(100)$ particles. Careful inspection of the space–time plots shows that there are two distinct wavy patterns present as indicated by the dashed and solid black lines in the panels. First, we observe a stripe pattern originating from small-amplitude waves with a wave length of $O(D_p)$, which are traveling downwards with an average speed equal to V_s as indicated by the black dashed lines. Recall from Fig. 2 that in the instantaneous snapshots of the spatial particle distribution relatively large structures are present with groups of particles moving collectively faster or slower than the mean sedimentation velocity. Because of the finite lateral domain size, there is also a finite number of such large structures passing through a horizontal plane. Random fluctuations in this number of passing structures will cause mild fluctuations in the local plane average velocity around the mean sedimentation velocity and, associated with this, mild fluctuations in the local plane average concentration. The stripe pattern is thus expected to gradually fade away when the horizontal dimensions of the computational domain are increased, though we have not tested this. Next to the stripe pattern, we observe larger-amplitude waves with a much larger wave length. We associate these waves with kinematic waves. They appear to travel upwards at a fraction of $|V_s|$ for $Ga = 144$ and 178, while moving slowly downwards for $Ga = 210$, as indicated by the black solid lines in the panels.

As already mentioned, the signal of Φ is rather noisy. The noise is responsible for a loss of spatio-temporal coherence of the kinematic waves. To isolate the component of Φ related to kinematic waves it seems therefore natural to apply an additional local time average that filters out the "high-frequency noise" while it preserves the low-frequency signal of the kinematic waves: $\hat{\Phi} = \int_{-T/2}^{T/2} \Phi(t+\tau)d\tau/T$ with T the filter width. The filter width should satisfy $\tau_{L,vv} \ll T \ll T_{KW}$, where T_{KW} is the kinematic wave period. In Appendix B we argue that $\hat{\Phi}$ is approximately governed by the following transport equation:

$$\frac{\partial \hat{\Phi}}{\partial t} + V_{KW}\frac{\partial \hat{\Phi}}{\partial y} \approx \frac{\partial}{\partial y}\left(\mathcal{D}_{yy}\frac{\partial \hat{\Phi}}{\partial y}\right), \tag{17a}$$

where $\mathcal{D}_{yy}$ is the particle diffusivity in the vertical given by Eq. (9) and $V_{KW} \approx \partial\left[V_s(\phi)\phi\right]/\partial\phi$ is the speed at which kinematic waves are propagating in the vertical (Kynch, 1952). Based on the Richardson–Zaki relation for V_s given by Eq. (1), which is valid for $\phi \gtrsim 10\%$, the kinematic wave speed can be further approximated by:

$$V_{KW} \approx \left[\frac{1-(n+1)\phi}{1-\phi}\right]V_s(\phi). \tag{17b}$$

where n is the power-law exponent in the Richardson–Zaki relation.

Instead of applying local time averaging to the space–time plots in Fig. 14, we use here the method of repeated space–time autocorrelations to visualize the spatio-temporal structure of the kinematic waves. The method is explained in detail in Appendix C. The main principle of the method is that the spatio-temporal structure of traveling waves is preserved in a space–time autocorrelation. By performing repeated autocorrelations, the dominant wave component is amplified relative to other less dominant components and "noise" is filtered out. We define the first autocorrelation as the ordinary autocorrelation of the raw signal and the nth autocorrelation as the autocorrelation of the $(n-1)$th autocorrelation. The rank n can be tuned to amplify the dominant traveling wave component to the desired degree, see Appendix C. An advantage of the repeated autocorrelation technique is that no a priori assumption is required on the properties of kinematic waves as compared to filtering in time, space, frequency and/or wave number space (Willen et al., 2017).

The right panels in Fig. 14 show the 7th space–time autocorrelation corresponding to the space–time plots of the plane average concentration in the left panels. From the smooth fields thus obtained, we determined the wave speed of the dominant kinematic wave from the slope of the least-squares regression line through the correlation maxima. The results are shown in Fig. 15(a). Kinematic waves travel always slower than the mean sedimentation velocity and their wave speed goes down with increasing concentration. Interestingly, in the range of $\phi = 20$–30% their velocity reduces to zero, corresponding to a standing wave, and they start to propagate upwards upon further increasing the bulk concentration as also visible from Figs. 14(b) and 14(d). The agreement with the model predictions from Eq. (17b) is reasonably good, especially for $Ga = 178$. The model overpredicts the normalized wave speed in the lower concentration range as well as at $\phi = 30\%$. We note that less good agreement has to be expected for the lower concentration range anyway, as the model is based on Eq. (1) that underestimates the sedimentation velocity for $\phi \lesssim 10\%$. Differences between the model and the DNS may also be related to model assumptions such as the quasi-steady response of the settling speed of the particles to changes in the local concentration and the assumption that perturbations in the local concentration are small relative to the bulk concentration. We have also determined the wave length of the dominant kinematic wave from the average vertical distance between consecutive maxima in the 7th space–time autocorrelation at zero time lag. Fig. 15(b) shows the result. Large variations in kinematic wave length can be observed, varying from about 5 to 40 particle diameters. At each Ga, the lowest wave length is found for $\phi = 30\%$. No clear trend can be seen in the dependency of the wave length of Ga.

In Section 4.6 we suggested that the oscillatory behavior observed in some of the correlations can be related to the possible presence of kinematic waves. Fig. 15(c) illustrates how the passage of vertically propagating, plane kinematic waves will periodically perturb the particles. The corresponding angular perturbation frequency is given by:

$$\omega_{KW} = \frac{2\pi|V_s - V_{KW}|}{\lambda_{KW}}. \tag{18}$$

In Fig. 16 we have plotted the peak frequencies of the particle velocity spectra shown in Fig. 12 as function of the bulk concentration for each investigated Galileo number. For comparison we also plotted the expected perturbation frequency from the kinematic waves as given by Eq. (18).

Interestingly, for $Ga = 144$ we find an almost perfect match of the expected kinematic wave frequency with the peak frequency of either the horizontal or the vertical velocity spectrum. For $\phi = 4$ and 10% there is a good match with both velocity spectra. Furthermore, when also considering the frequency of the second largest peak (not shown here), the match between the velocity spectra is further improved (e.g., for $\phi = 2\%$, the 2nd peak in the vertical velocity spectrum coincides with the peak frequency of the horizontal velocity spectrum). At $\phi = 25$ and 30% the agreement of the peak frequencies with the kinematic wave frequency is poor, but recall that the corresponding spectra vary smoothly without any distinct frequency peak. Different from $Ga = 144$, for $Ga = 178$ only a good match of the peak frequencies with the kinematic wave frequency is found for $\phi = 4\%$. For $\phi \geq 6\%$, the normalized kinematic wave frequency is beyond 0.1, which is in the range where for $Ga = 178$ the velocity spectra vary smoothly with frequency. At $Ga = 210$, a good match is found only for the lower concentration range till and with $\phi = 10\%$. To conclude, for all Ga, a good match is found only in the lower concentration range, where we expect that wake trapping and DKT-type instabilities are active. Based on this, we hypothesize that kinematic waves may trigger such instabilities at particle level, while conversely such instabilities

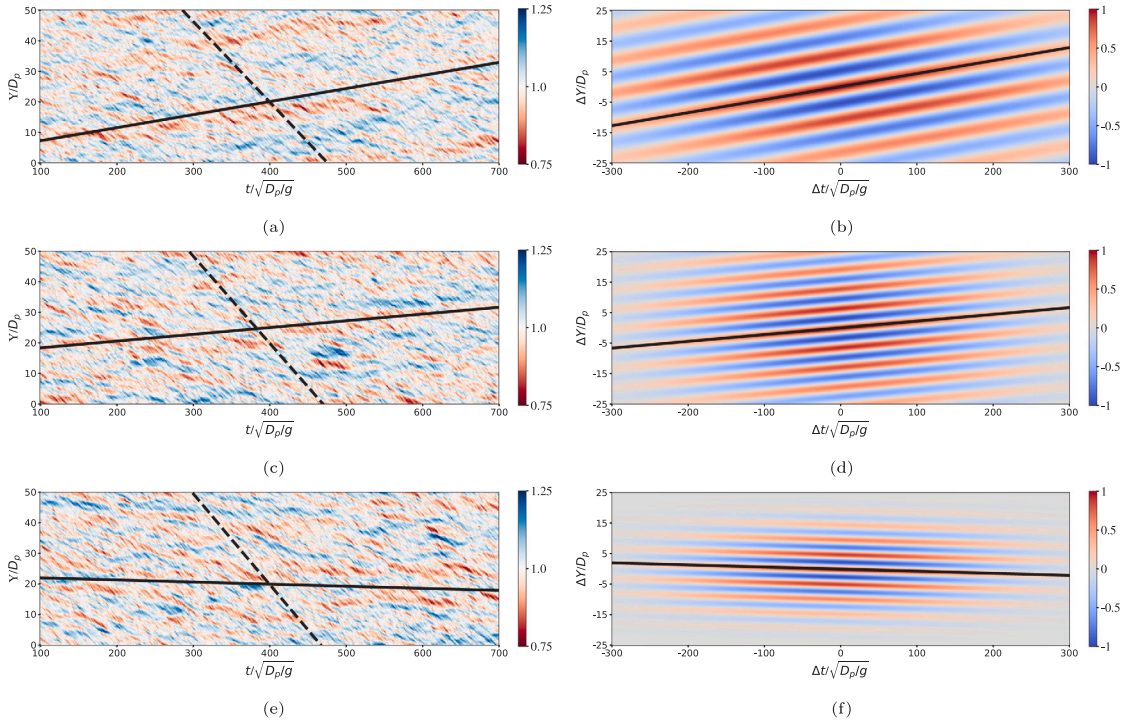

Fig. 14. (a), (c) and (e) Space–time plot of the instantaneous horizontal plane average concentration normalized with the bulk concentration, $\Phi(y,t)/\phi$, at $\phi = 30\%$ for $Ga = 144$, 178 and 210, respectively. The slope of the black lines corresponds to $V_s/\sqrt{gD_p}$ (dashed) and $V_{KW}/\sqrt{gD_p}$ (solid). (b), (d) and (f) Space–time plot of the 7th space–time autocorrelation of plane average concentration field shown in (a), (c) and (e), respectively. The slope of the black solid line corresponds to $V_{KW}/\sqrt{gD_p}$.

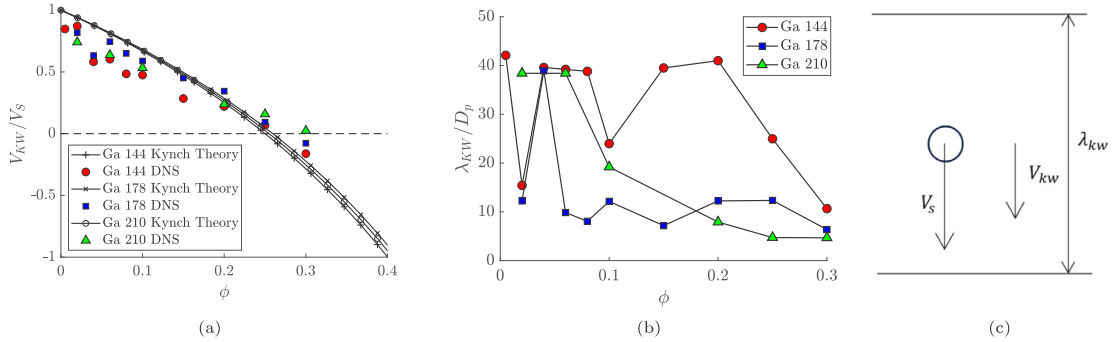

Fig. 15. (a) Kinematic wave speed normalized by the mean sedimentation velocity and shown as function of ϕ and Ga. Positive (negative) values correspond to downward (upward) traveling waves. Black lines represent the model predictions from Eq. (17b). (b) Kinematic wave length normalized with the particle diameter and shown as function of ϕ and Ga. (c) Illustration of the perturbation of a particle by the passage of a kinematic wave. On statistical average, the particles are moving with the mean sedimentation velocity V_s. The presence of vertically propagating plane kinematic waves with a wave length λ_{KW} and speed V_{KW} will periodically perturb the particles with an oscillation period of $\lambda_{KW}/|V_s - V_{KW}|$.

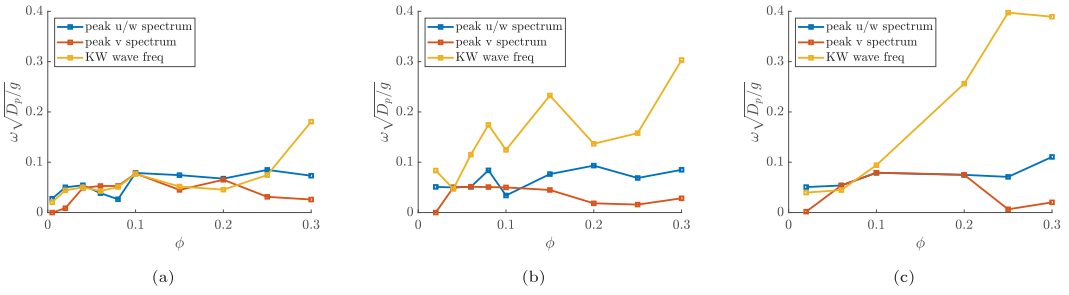

Fig. 16. Normalized frequencies of dominant peak in the frequency spectra of the particle velocity shown in Fig. 12, plotted as function of the bulk concentration. In the legend, u/w and v refer to the spectrum for the horizontal and the vertical velocity, respectively. The yellow line is the perturbation frequency from the passage of kinematic waves. (a) $Ga = 144$, (b) $Ga = 178$, (c) $Ga = 210$. (For interpretation of the references to color in this figure legend, the reader is referred to the web version of this article.)

may be responsible for the onset of kinematic waves. This is in line with our previous analysis of the lagged cross-correlations discussed in Section 4.6.

Finally, we assess from Eq. (17a) the effect of particle dispersion on damping of kinematic waves. To this purpose, we define a "kinematic wave dispersive damping number", $\mathcal{P}$, as the ratio of the advection to the diffusion time scale based on Eq. (17a):

$$\mathcal{P} = \frac{\lambda_{KW}/|V_{KW}|}{\lambda_{KW}^2/D_{yy}} = \frac{v_{p,rms}^2\,\tau_{L,vv}\,\omega_{KW}}{\pi\,|V_s - V_{KW}|\,|V_{KW}|}. \tag{19}$$

We found that $\mathcal{P} < 0.47$ for $\phi \leq 20\%$, while $\mathcal{P} > 0.63$ at $\phi = 25$ and 30% for all Ga. Dispersive damping may thus explain why no significant imprint of kinematic waves is found on the particle velocity spectra in the dense regime.

5. Conclusions and discussion

We presented DNS results for sedimenting suspensions of solid spheres in a viscous fluid. The particle/fluid density ratio was fixed at 1.5, while the bulk concentration was varied from 0.5%–30% and three different Galileo numbers were considered in the range of 144–210. Based on our comprehensive analysis, our main conclusions are:

(1) The suspension dynamics for $\phi = 2$–30% depends mostly on the bulk concentration, while at fixed bulk concentration qualitatively similar behavior is observed for all three Galileo numbers. In qualitative agreement with previous studies in literature (Yin and Koch, 2007; Uhlmann and Doychev, 2014), three concentration regimes with a different microstructure can be distinguished: (i) the dilute concentration regime for $\phi \lesssim 2\%$ with preferential settling of particles in vertical trains, (ii) the moderate concentrations regime for $2\% \lesssim \phi \lesssim 10\%$ with a preference of particles to settle side-by-side in horizontal particle pairs at a distance of $\sim 1.5D_p$, and (iii) the dense concentration regime for $\phi \gtrsim 10\%$ with a nearly random ("hard-sphere") distribution of the particles in space. The transition across regimes is gradual. For instance, for $\phi = 2\%$ we found an enhanced likelihood for settling in both vertical trains of a few particles and in horizontal particle pairs.

(2) The vertical trains in the dilute regime are formed by the wake-trapping mechanism. While for two isolated particles wake trapping is typically followed by a drafting–kissing–tumbling (DKT) instability, the vertical trains in dilute suspensions are rather stable, suggesting that "kissing" and "tumbling" is suppressed. The stability is reflected in the super-Gaussian pdf of the horizontal particle velocity. The negatively skewed pdf of the vertical particle velocity provides evidence of an enhanced settling speed of particles contained within the vertical trains. The formation of vertical trains is most pronounced for $Ga = 144$ and $\phi = 0.5\%$. At the same density ratio and bulk concentration, Uhlmann and Doychev (2014) found no significant change in the settling speed for $Ga = 121$ and a 12% increase for $Ga = 178$. Our result for $Ga = 144$ does not show enhanced settling, consistent with the presumed threshold of $Ga \approx 155$ for this to happen (Uhlmann and Doychev, 2014). With increasing concentration, the extent of the fluid wake behind the particles decreases rapidly and so does the extent of the vertical trains till they finally disappear at a bulk concentration of 2–4%. Multiparticle interactions might also contribute to destabilization and breakdown of the vertical clusters when the bulk concentration is increased.

(3) The particle-conditioned mean concentration and particle velocity field indicate that in the moderate concentration regime the horizontal particle pairs originate from a DKT-type instability. The active role of DKT in this regime is further supported by the strong anti-correlation peak in the autocorrelation and cross-correlation of the particle velocity fluctuations. The cross-correlation coefficient exhibits a clear peak in the lower concentration range, though the relatively low value below 0.2 suggests that DKT is not a very strong mechanism and has to compete with chaotic motions from multiparticle interactions. The decreasing extent of the fluid wake behind the particles and the increasing importance of multiparticle interactions might be responsible for gradual weakening of the DKT mechanism with increasing bulk concentration. Normalized with $\sqrt{gD_p}$ the particle rms velocity exhibits a Ga-dependent peak in the moderate concentration range, which underlines the importance of inertial hydrodynamic interactions between particles. The nearly Gaussian pdf of the particle velocity exhibits no sign of a significantly different average settling speed of the particle pairs compared to the mean sedimentation velocity.

(4) In the dense concentration regime particle velocity fluctuations are dominated by short-range multiparticle interactions. The observed asymmetry in the concentric ring-like pattern of the particle-conditioned mean concentration, with a higher preference for horizontal than for vertical particle alignment, suggests that DKT-type instabilities are still present, though weak and confined in space to an interparticle distance of about 1–2 particle diameters at $\phi = 30\%$. The anti-correlation peak in the autocorrelation and cross-correlation of the particle velocities is very small and consistent with weak and spatially confined DKT instabilities. The pdfs of the particle velocities exhibit a Gaussian distribution. The frequency spectra of the particle velocity fluctuations vary smoothly with frequency in the absence of distinct frequency peaks. Furthermore, they exhibit clear power-law scaling: the spectra of the vertical and horizontal velocity components scale with, respectively, ${\omega_*}^{-1.25}$ and ${\omega_*}^{-0.6}$ for $0.1 \lesssim \omega_* \lesssim 0.4$, and with, respectively, ${\omega_*}^{-2.75}$ and ${\omega_*}^{-3}$ for $\omega_* \gtrsim 0.4$. We proposed a model to explain the ${\omega_*}^{-3}$ scaling from the inertial response of the particles to small-scale fluid perturbations. It is left for future research to investigate the physical origin of the power-law scaling in more detail. The normalized frequency spectra are nearly independent of Ga in the dense regime, in particular for the low and the higher frequency range. The same holds for the particle rms velocities when normalized with $\sqrt{gD_p}$. This indicates that $\sqrt{gD_p}$ and $\sqrt{D_p/g}$ are the characteristic velocity and time scale for fluctuating particle motions in the dense regime, at least when the particle/fluid density ratio is kept constant. Particle collisions occur frequently but are gentle. Estimates of the impact Stokes number and the collision Reynolds number indicate that particle interactions are dominated by viscous lubrication rather than particle collisions.

(5) Kinematic waves have been detected in all investigated cases, though overlaid with noise from unrelated particle motions. The noise is likely responsible for a loss of spatio-temporal coherence of the waves. The wave speed found from the method of repeated autocorrelations is in reasonable agreement with the prediction from Kynch theory using the Richardson–Zaki relation for the mean sedimentation velocity. The kinematic waves have a clear imprint on the frequency spectra of the particle velocity for concentrations till $\phi \approx 10\%$, being responsible for peak frequencies of roughly $O(0.05)\sqrt{g/D_p}$. The oscillatory behavior of the autocorrelation and especially the cross-correlation of the particle velocity in the moderate concentration regime suggests that kinematic waves possibly trigger DKT-type instabilities, while conversely DKT-type instabilities might also generate kinematic waves. At the highest concentrations in the dense regime, we found no imprint of kinematic waves on the frequency spectra of the particle velocity. Weak DKT-type instabilities and strong dispersive damping might be the reason.

(6) The Richardson–Zaki relation, Eq. (1), provides a good fit to the DNS data for $\phi \gtrsim 10\%$, while it underestimates the mean sedimentation velocity in the lower concentration range with the deviation increasing for decreasing concentration. This substantiates the hypothesis of Yin and Koch (2007) that the Richardson–Zaki relation is associated with a "hard-sphere distribution" of the particles, and that DKT-type instabilities are responsible for the underestimation of the sedimentation velocity in the lower concentration range. We also found evidence of a power-law scaling in the bulk concentration of the particle rms velocity normalized with the mean sedimentation velocity, in particular for the dense regime.

It is striking that for given bulk concentration the suspension microstructure is qualitatively similar for all three Galileo numbers. While for a single settling particle the particle's wake structure is very different for the three investigated Galileo numbers (a steady axi-symmetric wake for $Ga = 144$, a steady planar oblique wake for $Ga = 178$, and an oscillating planar oblique wake for $Ga = 210$), in the moderate and dense concentration regime the fluid wake structure is actually very similar, see Fig. 4. This is likely related to physical obstruction and perturbation of the particle wake by nearby neighboring particles. Based on this we hypothesize that the wake structure is controlled by the bulk concentration instead of the Galileo number beyond a Ga-dependent threshold concentration at which the particle mean free path is of the same order as the extent of the wake of an isolated settling particle. When the extent of the wake is roughly estimated by $O(10\,D_p)$, we find from Eq. (15) a threshold concentration of about $O(1\%)$, which seems quite plausible. Indeed, we find fairly little influence of Ga on the wake structure for $\phi = 2\%$, while the microstructure and suspension behavior for $Ga = 144$ and $\phi = 0.5\%$ is quite different from the case of $Ga = 178$ and $\phi = 0.5\%$ studied by Uhlmann and Doychev (2014). It remains to be seen to what degree our classification and characterization of the different settling regimes hold for Galileo numbers outside the presently studied range. More in particular, inertial hydrodynamic particle interactions associated with wake trapping and DKT are expected to ultimately vanish when the Galileo number is gradually lowered towards the Stokes regime. The DNS results of Yin and Koch (2007) indicate that DKT and related preference for horizontal particle pair alignment are still present at $Ga = 11.5$ ($Re_T \approx 5$), while absent for $Ga \leq 6.3$ ($Re_T \lesssim 2$). Consequently, the range of the random "hard-sphere" distribution is extended towards significantly lower concentrations in the low (viscous-dominated and weakly inertial) Ga regime as compared to the $\gtrsim 10\%$ concentration range for the higher (inertia-dominated) Ga regime presently studied.

Finally, it would be interesting to study the effect of varying the particle/fluid density ratio on the different settling regimes. The density ratio is known to affect the wake and path of a single settling path beyond the steady oblique regime and will thus likely have an effect on the suspension dynamics in the dilute concentration regime. The density ratio also influences the particle response time and hence will likely influence inertial hydrodynamic particle interactions too.

Funding

This work is part of the research programme Topsector Water with Number ALWTW.2016.050, which is (partly) financed by the Dutch Research Council (NWO).

CRediT authorship contribution statement

Tariq Shajahan: Conceptualization, Data curation, Formal analysis, Investigation, Methodology, Software, Validation, Visualization, Writing – original draft. **Wim-Paul Breugem:** Conceptualization, Formal analysis, Funding acquisition, Investigation, Methodology, Project administration, Software, Supervision, Writing – review & editing.

Declaration of competing interest

The authors declare that they have no known competing financial interests or personal relationships that could have appeared to influence the work reported in this paper.

Data availability

The data that support the findings of this study are openly available in 4TU.ResearchData at https://doi.org/10.4121/1cc98fd6-8d50-4203-96c0-125020c4c242.

Acknowledgment

The authors would like to thank SURF (https://www.surf.nl) for using the Dutch National Supercomputer Snellius for performing the numerical simulations and data analysis.

Appendix A. Scaling of particle velocity spectra in the dense concentration regime

We adopt the following simple model for particle velocity fluctuations in the dense concentration regime:

$$\frac{dv_p'}{dt} = \beta f' - \frac{(v_p' - v_q')}{\tau_p}, \tag{A.1}$$

where the term on the left hand side accounts for the effect of particle inertia and added mass, the first term on the right hand side accounts for forcing by fluid pressure and viscous stress fluctuations, with β a dimensionless function of the particle-to-fluid density ratio and particle volume fraction and f' the fluctuating hydrodynamic force per unit particle mass, and the last term on the right hand side accounts for lubrication interactions with neighboring particles with a typical velocity fluctuation v_q' and with τ_p an apparent time scale at which viscous lubrication acts.

Assuming that the particle velocity fluctuations are uncorrelated with the velocity fluctuations of neighboring particles, the following equation can be derived for the temporal autocovariance of the particle velocity fluctuations:

$$\frac{d^2 R_{vv}}{d\tau^2} - \frac{R_{vv}}{\tau_p^2} = -\beta^2 R_{ff}, \tag{A.2}$$

where R_{ff} is the temporal autocovariance of f'. By taking the Fourier transform of this equation, we can relate the frequency spectrum of the particle velocity to the frequency spectrum of the fluid forcing:

$$E_{vv}(\omega) = \frac{\beta^2 \tau_p^2}{1 + (\omega\tau_p)^2} \cdot E_{ff}(\omega). \tag{A.3}$$

To model the forcing spectrum for the higher-frequency range, we assume that the forcing perturbations originate from small-scale fluid velocity perturbations ahead of the particle that are transported with the mean relative fluid velocity towards the particle and subsequently blocked and deflected by the particle. This yields a force perturbation on the particle of $f' = O(V_r \partial v_f'/\partial y)$ with $V_r = -V_s/(1-\phi)$ the mean relative fluid velocity. Similar to Taylor's hypothesis of frozen turbulence (Nieuwstadt et al., 2016), we assume that the fluid velocity perturbations are rapidly advected past the particle compared to their lifetime. We can thus relate the forcing spectrum to the wavenumber spectrum of fluid velocity perturbations, $F(k)$, as follows:

$$E_{ff}(\omega) \propto \frac{(V_r k)^2 F(k)}{V_r}, \tag{A.4}$$

where the wavenumber k of the fluid perturbations relates to the frequency ω of particle perturbations as $k = \omega/V_r$.

For bubble-induced agitation of the fluid in homogeneous bubble swarms, Lance and Bataille (1991), Risso (2018) used the spectral energy balance to argue that $F(k) \sim \epsilon k^{-3}/\nu_f$ for sufficiently large k, where

ϵ is the viscous dissipation rate per unit fluid mass. A similar scaling based on the same argumentation is expected to hold for sedimenting sphere suspensions. Eq. (A.3) then becomes:

$$E_{vv}(\omega) \propto \frac{\beta^2(\omega\tau_p)^2}{1+(\omega\tau_p)^2} \cdot \frac{\epsilon V_{fr}^2}{\nu_f \omega^3} . \tag{A.5}$$

Finally, two frequency limits can be considered:

$$\omega\tau_p \ll 1 \ : \ E_{vv}(\omega) \propto \left(\frac{\beta^2 \epsilon V_{fr}^2 \tau_p^3}{\nu_f}\right) \cdot \left(\omega\tau_p\right)^{-1} , \tag{A.6a}$$

$$\omega\tau_p \gg 1 \ : \ E_{vv}(\omega) \propto \left(\frac{\beta^2 \epsilon V_{fr}^2 \tau_p^3}{\nu_f}\right) \cdot \left(\omega\tau_p\right)^{-3} . \tag{A.6b}$$

In the dense concentration regime, the characteristic velocity and time scale are proportional to $\sqrt{gD_p}$ (Fig. 6.a) and $\sqrt{D_p/g}$ (Fig. 10), respectively. We thus expect that $\epsilon \propto \nu_f g/D_p$, $\tau_p \propto \sqrt{D_p/g}$ and the pre-factor at the right-hand side of the above equation to be proportional with $\sqrt{gD_p^3}$. In fact, the change in scaling behavior of the velocity spectra at $\omega\sqrt{D_p/g} \approx 0.4$ suggests that $\tau_p \approx 2.5\sqrt{D_p/g}$ for the currently investigated particle-to-fluid density ratio of 1.5. Thus, the above equation can be rewritten into the following form:

$$\omega\sqrt{D_p/g} \ll 0.4 \ : \ \frac{E_{vv}}{\sqrt{gD_p^3}} \propto \left(\omega\sqrt{D_p/g}\right)^{-1} , \tag{A.7a}$$

$$\omega\sqrt{D_p/g} \gg 0.4 \ : \ \frac{E_{vv}}{\sqrt{gD_p^3}} \propto \left(\omega\sqrt{D_p/g}\right)^{-3} , \tag{A.7b}$$

which for the high-frequency limit is in very close agreement with the observed scaling of the spectra in Fig. 12, though with a slightly less steep slope (−2.75 vs −3) for the vertical velocity fluctuations. For the lower-frequency range, the model prediction is less good, likely because the k^{-3} scaling of F does only hold for sufficiently large k (Lance and Bataille, 1991). For $0.1 \lesssim \omega \lesssim 0.4$ the fluid forcing seems anisotropic as the power-law scaling for the horizontal and vertical velocity spectra are different. The fact that their power-law exponents differ by a factor 2 suggests that the forcing of the two velocity components is still related to the same mechanism. We speculate that this could be a local DKT-type interaction between particles, but it is left for future study to test this hypothesis.

Appendix B. Mass balance equation for plane average concentration

We define the horizontal plane average concentration by $\Phi(y,t) = \langle\gamma\rangle_h$, where $\gamma(x,y,z,t)$ is the solid phase indicator function (equal to 1 in the solids and 0 in the fluid) and the brackets with subscript h denote the average over the horizontal directions in the computational domain (x and z). In a similar vein, we define the intrinsic plane average of the vertical particle velocity by $V_i = \langle\gamma v_p\rangle_h/\Phi$. Mass conservation requires that:

$$\frac{\partial \Phi}{\partial t} + \frac{\partial \left(V_i \Phi\right)}{\partial y} = 0 . \tag{B.1}$$

From Fig. 14 we observe that Φ is a rather noisy signal. To isolate the component of Φ related to kinematic waves, we introduce a local time average defined by $\widehat{\Phi} = \int_{-T/2}^{T/2} \Phi(t+\tau)d\tau/T$. We require that the filter width T is much larger than the integral time scale of the fluctuations in the vertical particle velocity ($\tau_{L,vv}$) on the one hand, while much smaller than the period of the kinematic waves (T_{KW}) on the other hand: $\tau_{L,vv} \ll T \ll T_{KW}$. When this condition is satisfied, the local time average preserves the signal related to low-frequency kinematic waves, while high-frequency "noise" is filtered out. We now decompose Φ and V_i according to $\Phi = \widehat{\Phi} + \widetilde{\Phi}$ and $V_i = \widehat{V}_i + \widetilde{V}_i$, where the tilde symbol denotes the deviation from the local time average. Application of the local time average to Eq. (B.1) yields the following result:

$$\frac{\partial \widehat{\Phi}}{\partial t} + \frac{\partial \left(\widehat{V}_i \widehat{\Phi}\right)}{\partial y} = -\frac{\partial \widehat{\widetilde{V}_i \widetilde{\Phi}}}{\partial y} . \tag{B.2}$$

Assuming that the local time and plane average particle velocity is in quasi-steady equilibrium with the local time and plane average concentration (Kynch, 1952), we use the approximation $\widehat{V}_i \approx V_s(\widehat{\Phi})$ (i.e., $\widehat{V}_i$ is equal to the mean sedimentation velocity of a spatially uniform suspension with a concentration $\widehat{\Phi}$). Based on a similar analysis as in chapter 10 of Nieuwstadt et al. (2016), we approximate the flux at the right-hand side by:

$$-\widehat{\widetilde{V}_i \widetilde{\Phi}} \approx D_{yy} \frac{\partial \widehat{\Phi}}{\partial y} , \tag{B.3}$$

where D_{yy} is the particle diffusivity in the vertical given by Eq. (9). Provided that there are no shock discontinuities and hence that $\widehat{\Phi}$ is smoothly varying in space, we may write Eq. (B.2) into the following form (cf. Eq. 3.18 in Batchelor (1988)):

$$\frac{\partial \widehat{\Phi}}{\partial t} + V_{KW} \frac{\partial \widehat{\Phi}}{\partial y} \approx \frac{\partial}{\partial y}\left(D_{yy} \frac{\partial \widehat{\Phi}}{\partial y}\right) , \tag{B.4}$$

where $V_{KW} = \partial\left[V_s(\widehat{\Phi})\widehat{\Phi}\right]/\partial\widehat{\Phi}$ is the speed at which kinematic waves are propagating in the vertical (Kynch, 1952). Finally, we assume that variations in $\widehat{\Phi}$ are small compared to the bulk concentration ϕ, so that we may approximate V_{KW} by Batchelor (1988):

$$V_{KW} \approx \left[\frac{1-(n+1)\phi}{1-\phi}\right] V_s(\phi) . \tag{B.5}$$

where n is the power-law exponent in Eq. (1) for $V_s(\phi)$, valid for $\phi \gtrsim 10\%$.

Appendix C. Method of repeated space–time autocorrelations

The principle of the proposed method is that traveling wave characteristics of kinematic waves are preserved in the space–time autocorrelation of a space–time concentration field, while uncorrelated noise is filtered out. In addition, the "rank" of the autocorrelation can be tuned to amplify traveling wave modes when their contribution to the variance of the original signal is weak and to determine which wave mode is dominant. We define the first autocorrelation as the standard autocorrelation of a concentration field, and the second autocorrelation as the autocorrelation of the first autocorrelation. More in general, we define the nth autocorrelation as the autocorrelation of the $(n-1)$th autocorrelation. To illustrate how the method works, we decompose the fluctuating, plane-averaged concentration, $\Phi'(y,t)$, into N traveling sine waves with amplitude A_l, wave speed c_l and phase θ_l, and a remaining term $\mathcal{N}$:

$$\Phi'(y,t) = \sum_{l=0}^{N-1} A_l \sin([y - c_l t]k_l + \theta_l) + \mathcal{N}(y,t) . \tag{C.1}$$

Note that for $c_l = 0$, $\mathcal{N} = 0$, and N equal to the number of grid cells in the periodic y-direction, Eq. (C.1) is essentially the Discrete Fourier Transform of Φ' at a given time. The variation of Φ' in time is thus accounted for by non-zero values of c_l and $\mathcal{N}$. Below we will determine the autocorrelations for the model signal given by Eq. (C.1) under the assumption that $\mathcal{N}$ can be modeled by white noise.

The first space–time autocorrelation of the above model signal can be computed by first computing the autocovariance, $R_1(\check{y},\check{t})$, with $\check{y}$ and $\check{t}$ denoting the spatial and temporal lag, respectively, and then normalizing it with the variance $R_1(0,0)$. In preliminary form, the autocovariance is given by:

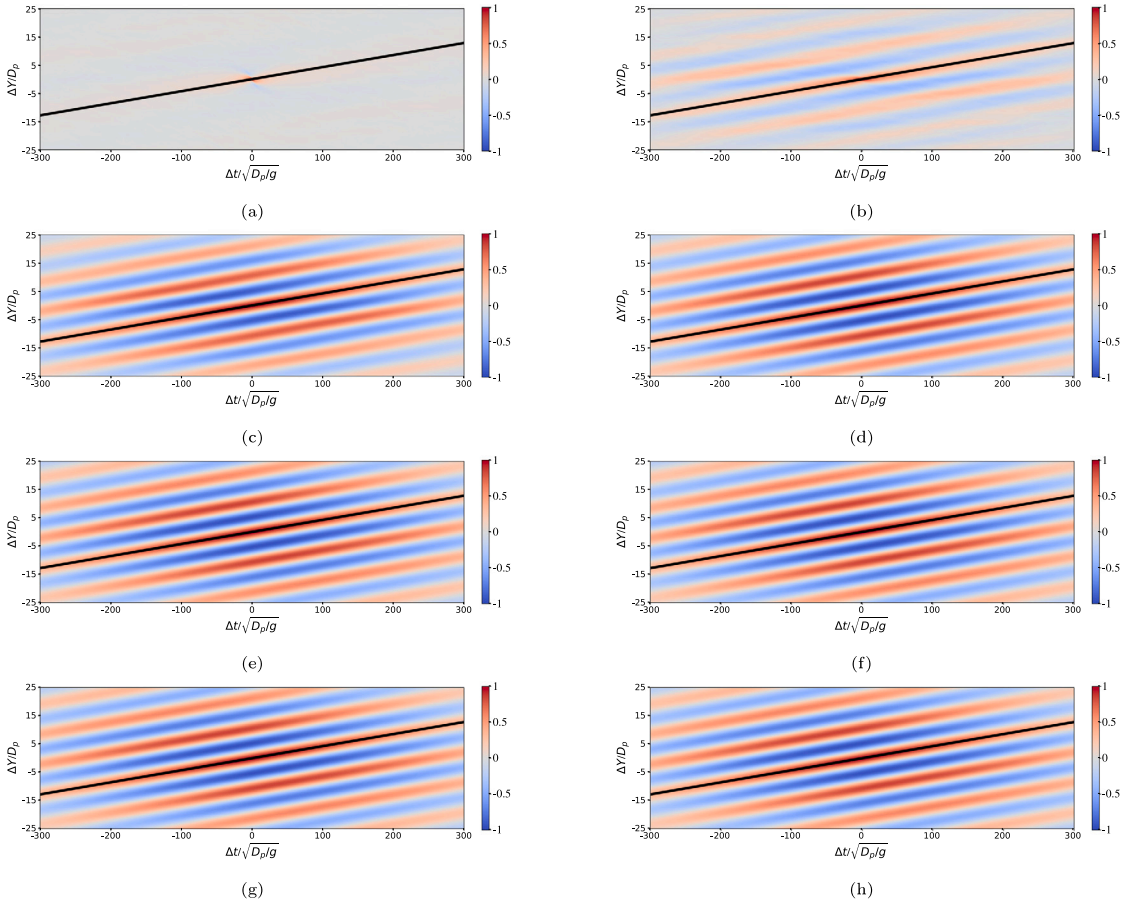

Fig. C.1. Illustration of the method of repeated autocorrelations applied to the plane-averaged concentration field of the case with $Ga = 144$ and $\phi = 30\%$, see also Fig. 14a, b. The slope of the black solid line corresponds to $V_{KW}/\sqrt{gD_p}$ determined from the 7th autocorrelation. (a)–(h) First till and with eighth autocorrelation.

$$R_1(\check{y},\check{t}) = \frac{1}{T\,L}\int_{t=0}^{T}\int_{y=0}^{L}\sum_{l=0}^{N-1}\sum_{q=0}^{N-1} A_l A_q \Big[\sin\left([y-c_l t]k_l+\theta_l\right)\Big] \times \Big[\sin\left([y+\check{y}-c_q(t+\check{t})]k_q+\theta_q\right)\Big] dy\,dt + R_{\mathcal{N}}(\check{y},\check{t}), \tag{C.2a}$$

where

$$R_{\mathcal{N}}(\check{y},\check{t}) = \begin{cases} \sigma_{\mathcal{N}}^2 & \text{for } \check{y}=\check{t}=0, \\ 0 & \text{otherwise}. \end{cases} \tag{C.2b}$$

Here L is the height of the periodic domain and the integration time T is sufficiently large such that an integer number of periods of every wave component is captured. The integral in Eq. (C.2a) is only nonzero for $l = q$ and hence we can write R_1 as the sum of the following components:

$$R_1(\check{y},\check{t}) = R_{11}(\check{y},\check{t}) + R_{12}(\check{y},\check{t}) + R_{13}(\check{y},\check{t}) + R_{14}(\check{y},\check{t}) + R_{\mathcal{N}}(\check{y},\check{t}), \tag{C.3}$$

with the components R_{11} till and with R_{14} given by:

$$\begin{aligned} R_{11}(\check{y},\check{t}) &= \frac{1}{T\,L}\int_{t=0}^{T}\int_{y=0}^{L}\sum_{l=0}^{N-1} A_l^2\Big[\sin\left([y-c_l t]k_l\right)\Big]\cos\left(\theta_l\right) \times\Big[\sin\left([y-c_l t]k_l+\theta_l\right)\cos\left([\check{y}-c_l\check{t}\,]k_l\right)\Big]dy\,dt, \\ &= \sum_{l=0}^{N-1}\frac{1}{2}A_l^2\cos^2\left(\theta_l\right)\cos\left([\check{y}-c_l\check{t}\,]k_l\right), \end{aligned} \tag{C.4a}$$

$$\begin{aligned} R_{12}(\check{y},\check{t}) &= \frac{1}{T\,L}\int_{t=0}^{T}\int_{y=0}^{L}\sum_{l=0}^{N-1} A_l^2\Big[\cos\left([y-c_l t]k_l\right)\Big]\sin\left(\theta_l\right) \times\Big[\sin\left([y-c_l t]k_l+\theta_l\right)\cos\left([\check{y}-c_l\check{t}\,]k_l\right)\Big]dy\,dt, \\ &= \sum_{l=0}^{N-1}\frac{1}{2}A_l^2\sin^2\left(\theta_l\right)\cos\left([\check{y}-c_l\check{t}\,]k_l\right), \end{aligned} \tag{C.4b}$$

$$\begin{aligned} R_{13}(\check{y},\check{t}) &= \frac{1}{T\,L}\int_{t=0}^{T}\int_{y=0}^{L}\sum_{l=0}^{N-1} A_l^2\Big[\sin\left([y-c_l t]k_l\right)\Big]\cos\left(\theta_l\right) \times\Big[\cos\left([y-c_l t]k_l+\theta_l\right)\sin\left([\check{y}-c_l\check{t}\,]k_l\right)\Big]dy\,dt, \\ &= -\sum_{l=0}^{N-1}\frac{1}{4}A_l^2\sin\left(2\theta_l\right)\sin\left([\check{y}-c_l\check{t}\,]k_l\right), \end{aligned} \tag{C.4c}$$

$$\begin{aligned} R_{14}(\check{y},\check{t}) &= \frac{1}{T\,L}\int_{t=0}^{T}\int_{y=0}^{L}\sum_{l=0}^{N-1} A_l^2\Big[\cos\left([y-c_l t]k_l\right)\Big]\sin\left(\theta_l\right) \times\Big[\cos\left([y-c_l t]k_l+\theta_l\right)\sin\left([\check{y}-c_l\check{t}\,]k_l\right)\Big]dy\,dt, \\ &= \sum_{l=0}^{N-1}\frac{1}{4}A_l^2\sin\left(2\theta_l\right)\sin\left([\check{y}-c_l\check{t}\,]k_l\right). \end{aligned} \tag{C.4d}$$

By summing up the contributions, we obtain the following expressions for the autocovariance and variance, respectively:

$$R_1(\check{y},\check{t}) = \sum_{l=0}^{N-1}\frac{1}{2}A_l^2\cos\left([\check{y}-c_l\check{t}\,]k_l\right) + R_{\mathcal{N}}(\check{y},\check{t}), \tag{C.5a}$$

$$R_1(0,0) = \sum_{l=0}^{N-1}\frac{1}{2}A_l^2 + \sigma_{\mathcal{N}}^2. \tag{C.5b}$$

Finally, the first space–time autocorrelation is obtained by dividing Eq. (C.5a) by Eq. (C.5b):

$$\rho_1(\check{y},\check{t}) = \sum_{l=0}^{N-1} A_{l,1}\cos\left([\check{y}-c_l\hat{t}\,]k_l\right) + \rho_{\mathcal{N}}(\hat{y},\hat{t}), \tag{C.6a}$$

$$A_{l,1} = \frac{A_l^2}{\sum_{q=0}^{N-1} A_q^2 + 2\sigma_{\mathcal{N}}^2} \qquad \rho_{\mathcal{N}} = \frac{2R_{\mathcal{N}}}{\sum_{q=0}^{N-1} A_q^2 + 2\sigma_{\mathcal{N}}^2}\,. \tag{C.6b}$$

We remark that $\rho_{\mathcal{N}}(\hat{y},\hat{t}) \neq 0$ only when $\hat{y} = \hat{t} = 0$ as white noise correlates with itself only for zero displacement.

The second space–time autocorrelation is computed in a similar manner and is equal to:

$$\rho_2(\hat{y},\hat{t}) = \sum_{l=0}^{N-1} A_{l,2} \cos\left([\hat{y} - c_l\hat{t}\,]k_l\right)\,, \tag{C.7a}$$

$$A_{l,2} = \frac{A_{l,1}^2}{\sum_{q=0}^{N-1} A_{q,1}^2} = \frac{A_l^4}{\sum_{q=0}^{N-1} A_q^4}\,. \tag{C.7b}$$

The second autocorrelation can be readily generalized to the nth space–time autocorrelation, which for $n > 1$ reads:

$$\rho_n(\hat{y},\hat{t}) = \sum_{l=0}^{N-1} A_{l,n} \cos\left([\hat{y} - c_l\hat{t}\,]k_l\right) \quad \text{for } n > 1\,, \tag{C.8a}$$

$$A_{l,n} = \frac{A_l^{(2^n)}}{\sum_{q=0}^{N-1} A_q^{(2^n)}}\,. \tag{C.8b}$$

The higher-rank autocorrelation maintains the traveling wave characteristics of the original signal. In addition, the higher the rank of the autocorrelation, the more the dominant traveling wave mode is amplified with respect to less dominant traveling wave modes. Let l_1 and l_2 be the dominant and second dominant traveling wave mode, then the nth autocorrelation amplifies the dominant traveling wave mode by a factor $\left(A_1/A_2\right)^{(2^n)}$ relative to the second dominant mode. So even in the presence of weak traveling wave modes and/or modes with nearly similar amplitude, the rank of the autocorrelation may be tuned to amplify traveling wave signals and to determine which mode stands out over other possibly present modes. Another benefit of the method of repeated autocorrelations is that it requires no a priori assumption on the range in wave number (k_l) and frequency ($c_l k_l$) of the dominant traveling wave modes as compared to, e.g., spectral band-pass filter methods. The method of repeated autocorrelations is illustrated in Fig. C.1 for $Ga = 144$ and $\phi = 30\%$, showing the first till and with the eighth space–time autocorrelation of the plane-averaged concentration field. As is clearly visible, the correlations are nearly identical for rank three and higher, as expected from the theoretical example discussed above. We picked the seventh autocorrelation for determining the kinematic wave velocity and wave length in the present study to make sure that only the most dominant wave mode was left in the data.

References

Abraham, F.F., 1970. Functional dependence of drag coefficient of a sphere on Reynolds number. Phys. Fluids 13 (8), 2194–2195.

Auguste, F., Magnaudet, J., 2018. Path oscillations and enhanced drag of light rising spheres. J. Fluid Mech. 841, 228–266.

Barnea, E., Mizrahi, J., 1973. A generalized approach to the fluid dynamics of particulate systems: Part 1. General correlation for fluidization and sedimentation in solid multiparticle systems. Chem. Eng. J. 5 (2), 171–189.

Batchelor, G.K., 1972. Sedimentation in a dilute dispersion of spheres. J. Fluid Mech. 52 (2), 245–268.

Batchelor, G.K., 1988. A new theory of the instability of a uniform fluidized bed. J. Fluid Mech. 193, 75–110.

Batchelor, G., Wen, C.-S., 1982. Sedimentation in a dilute polydisperse system of interacting spheres. Part 2. Numerical results. J. Fluid Mech. 124, 495–528.

Breugem, W.-P., 2012. A second-order accurate immersed boundary method for fully resolved simulations of particle-laden flows. J. Comput. Phys. 231 (13), 4469–4498.

Climent, E., Maxey, M., 2003. Numerical simulations of random suspensions at finite Reynolds numbers. Int. J. Multiph. Flow 29 (4), 579–601.

Costa, P., Boersma, B.J., Westerweel, J., Breugem, W.-P., 2015. Collision model for fully resolved simulations of flows laden with finite-size particles. Phys. Rev. E 92, 053012.

Dance, S., Maxey, M., 2003. Incorporation of lubrication effects into the force-coupling method for particulate two-phase flow. J. Comput. Phys. 189 (1), 212–238.

Davis, R.H., Acrivos, A., 1985. Sedimentation of noncolloidal particles at low Reynolds numbers. Annu. Rev. Fluid Mech. 17 (1), 91–118.

Davis, R., Birdsell, K., 1988. Hindered settling of semidilute monodisperse and polydisperse suspensions. AIChE J. 34 (1), 123–129.

Davis, R., Serayssol, J.-M., Hinch, E., 1986. The elastohydrodynamic collision of two spheres. J. Fluid Mech. 163, 479–497.

Di Felice, R., Parodi, E., 1996. Wall effects on the sedimentation velocity of suspensions in viscous flow. AIChE J. 42 (4), 927–931.

El-Kaissy, M., Homsy, G., 1976. Instability waves and the origin of bubbles in fluidized beds: Part 1: Experiments. Int. J. Multiph. Flow. 2 (4), 379–395.

Esteghamatian, A., Hammouti, A., Lance, M., Wachs, A., 2017. Particle resolved simulations of liquid/solid and gas/solid fluidized beds. Phys. Fluids 29 (3), 033302.

Fabre, D., Tchoufag, J., Magnaudet, J., 2012. The steady oblique path of buoyancy-driven disks and spheres. J. Fluid Mech. 707, 24–36.

Fadlun, E., Verzicco, R., Orlandi, P., Mohd-Yusof, J., 2000. Combined immersed-boundary finite-difference methods for three-dimensional complex flow simulations. J. Comput. Phys. 161 (1), 35–60.

Felice, R.D., 1999. The sedimentation velocity of dilute suspensions of nearly monosized spheres. Int. J. Mult. Flow 25, 559–574.

Fornari, W., Picano, F., Brandt, L., 2016a. Sedimentation of finite-size spheres in quiescent and turbulent environments. J. Fluid Mech. 788, 640–669.

Fornari, W., Picano, F., Sardina, G., Brandt, L., 2016b. Reduced particle settling speed in turbulence. J. Fluid Mech. 808, 153–167.

Fortes, A.F., Joseph, D.D., Lundgren, T.S., 1987. Nonlinear mechanics of fluidization of beds of spherical particles. J. Fluid Mech. 177, 467–483.

Garside, J., Al-Dibouni, M.R., 1977. Velocity-voidage relationships for fluidization and sedimentation in solid-liquid systems. Ind. Eng. Chem. Process Des. Dev. 16 (2), 206–214.

Guazzelli, E., Hinch, J., 2011. Fluctuations and instability in sedimentation. Annu. Rev. Fluid Mech. 43, 97–116.

Guazzelli, E., Morris, J.F., 2012. A Physical Introduction to Suspension Dynamics. Cambridge University Press.

Hamid, A., Molina, J.J., Yamamoto, R., 2013. Sedimentation of non-Brownian spheres at high volume fractions. Soft Matter 9 (42), 10056–10068.

Hamid, A., Molina, J.J., Yamamoto, R., 2014. Direct numerical simulations of sedimenting spherical particles at non-zero Reynolds number. RSC Adv. 4, 53681–53693.

Horowitz, M., Williamson, C., 2010. The effect of Reynolds number on the dynamics and wakes of freely rising and falling spheres. J. Fluid Mech. 651, 251–294.

Huisman, S.G., Barois, T., Bourgoin, M., Chouippe, A., Doychev, T., Huck, P., Morales, C.E.B., Uhlmann, M., Volk, R., 2016. Columnar structure formation of a dilute suspension of settling spherical particles in a quiescent fluid. Phys. Rev. Fluids 1, 074204.

Jackson, R., 2000. The Dynamics of Fluidized Particles. Cambridge University Press.

Jayaweera, K.O.L.F., Mason, B.J., Slack, G.W., 1964. The behaviour of clusters of spheres falling in a viscous fluid. Part 1. Experiment. J. Fluid Mech. 20 (1), 121–128.

Jenny, M., Dušek, J., Bouchet, G., 2004. Instabilities and transition of a sphere falling or ascending freely in a Newtonian fluid. J. Fluid Mech. 508, 201–239.

Jeong, J., Hussain, F., 1995. On the identification of a vortex.. J. Fluid Mech. 285, 69–94.

Joseph, G.G., Hunt, M.L., 2004. Oblique particle–wall collisions in a liquid. J. Fluid Mech. 510, 71—93.

Kajishima, T., 2004. Influence of particle rotation on the interaction between particle clusters and particle-induced turbulence. Int. J. Heat Fluid Flow 25 (5), 721–728.

Kajishima, T., Takiguchi, S., 2002. Interaction between particle clusters and particle-induced turbulence. Int. J. Heat Fluid Flow 23 (5), 639–646.

Koch, D.L., 1993. Hydrodynamic diffusion in dilute sedimenting suspensions at moderate Reynolds numbers. Phys. Fluids 5 (5), 1141–1155.

Kynch, G.J., 1952. A theory of sedimentation. Trans. Faraday Soc. 48, 166–176.

Kytömaa, H., Brennen, C., 1991. Small amplitude kinematic wave propagation in two-component media. Int. J. Multiph. Flow. 17 (1), 13–26.

Ladd, A.J., 1993. Dynamical simulations of sedimenting spheres. Phys. Fluids 5 (2), 299–310.

Lance, M., Bataille, J., 1991. Turbulence in the liquid phase of a uniform bubbly air–water flow. J. Fluid Mech. 222, 95–118.

Legendre, D., Zenit, R., Daniel, C., Guiraud, P., 2006. A note on the modelling of the bouncing of spherical drops or solid spheres on a wall in viscous fluid. Chem. Eng. Sci. 61 (11), 3543–3549.

Luo, K., Wang, Z., Fan, J., Cen, K., 2007. Full-scale solutions to particle-laden flows: Multidirect forcing and immersed boundary method. Phys. Rev. E 76 (6), 066709.

Maxey, M., 2017. Simulation methods for particulate flows and concentrated suspensions. Annu. Rev. Fluid Mech. 49 (1), 171–193.

Nieuwstadt, F., Westerweel, J., Boersma, B., 2016. Introduction to Theory and Applications of Turbulent Flows. Springer.

Phillips, R., Brady, J., Bossis, G., 1988. Hydrodynamic transport properties of hard-sphere dispersions. I. Suspensions of freely mobile particles. Phys. Fluids 31 (12), 3462–3472.

Prosperetti, A., Tryggvason, G., 2009. Computational Methods for Multiphase Flow. Cambridge University Press.

Raaghav, S.K., Poelma, C., Breugem, W.-P., 2022. Path instabilities of a freely rising or falling sphere. Int. J. Multiph. Flow. 153, 104111.
Richardson, J.F., Zaki, W.N., 1954. Sedimentation and fluidization: part I. Trans. Inst. Chem. Eng. 32, 35–53.
Risso, F., 2018. Agitation, mixing, and transfers induced by bubbles. Annu. Rev. Fluid Mech. 50, 25–48.
Roma, A.M., Peskin, C.S., Berger, M.J., 1999. An adaptive version of the immersed boundary method. J. Comput. Phys. 153 (2), 509–534.
Seyed-Ahmadi, A., Wachs, A., 2021. Sedimentation of inertial monodisperse suspensions of cubes and spheres. Phys. Rev. Fluids 6 (4), 044306.
Shajahan, T., Breugem, W.-P., 2020. Influence of concentration on sedimentation of a dense suspension in a viscous fluid. Flow Turbul. Combust. 105 (2), 537–554.
Uhlmann, M., 2005. An immersed boundary method with direct forcing for the simulation of particulate flows. J. Comput. Phys. 209 (2), 448–476.
Uhlmann, M., Doychev, T., 2014. Sedimentation of a dilute suspension of rigid spheres at intermediate galileo numbers: the effect of clustering upon the particle motion. J. Fluid Mech. 752, 310–348.
Uhlmann, M., Dušek, J., 2014. The motion of a single heavy sphere in ambient fluid: A benchmark for interface-resolved particulate flow simulations with significant relative velocities. Int. J. Multiph. Flow. 59, 221–243.
van der Hoef, M., Ye, M., van Sint Annaland, M., Andrews, A., Sundaresan, S., Kuipers, J., 2006. Multiscale modeling of gas-fluidized beds. In: Marin, G.B. (Ed.), Computational Fluid Dynamics. In: Advances in Chemical Engineering, Vol. 31, Academic Press, pp. 65–149.
Veldhuis, C., Biesheuvel, A., 2007. An experimental study of the regimes of motion of spheres falling or ascending freely in a Newtonian fluid. Int. J. Multiph. Flow 33 (10), 1074–1087.
Wertheim, M., 1963. Exact solution of the percus-yevick integral equation for hard spheres. Phys. Rev. Lett. 10 (8), 321.
Wesseling, P., 2001. Principles of Computational Fluid Dynamics. Springer-Verlag.
Willen, D., Prosperetti, A., 2019. Resolved simulations of sedimenting suspensions of spheres. Phys. Rev. Fluids 4 (1), 014304.
Willen, D., Sierakowski, A., Zhou, G., Prosperetti, A., 2017. Continuity waves in resolved-particle simulations of fluidized beds. Phys. Rev. Fluids 2, 114305.
Wu, J., Manasseh, R., 1998. Dynamics of dual-particles settling under gravity. Int. J. Multiph. Flow. 24 (8), 1343–1358.
Yao, Y., Criddle, C.S., Fringer, O.B., 2021. The effects of particle clustering on hindered settling in high-concentration particle suspensions. J. Fluid Mech. 920, A40.
Yin, X., Koch, D.L., 2007. Hindered settling velocity and microstructure in suspensions of solid spheres with moderate Reynolds numbers. Phys. Fluids 19 (9), 093302.
Yin, X., Koch, D.L., 2008. Velocity fluctuations and hydrodynamic diffusion in finite-Reynolds-number sedimenting suspensions. Phys. Fluids 20 (4), 043305.
Zaidi, A.A., 2018. Particle velocity distributions and velocity fluctuations of non-Brownian settling particles by particle-resolved direct numerical simulation. Phys. Rev. E 98, 053103.
Zaidi, A.A., Tsuji, T., Tanaka, T., 2014. Direct numerical simulation of finite sized particles settling for high Reynolds number and dilute suspension. Int. J. Heat Fluid Flow 50, 330–341.
Zaidi, A.A., Tsuji, T., Tanaka, T., 2015. Hindered settling velocity & structure formation during particle settling by direct numerical simulation. Procedia Eng. 102, 1656–1666.
Zhou, W., Dušek, J., 2015. Chaotic states and order in the chaos of the paths of freely falling and ascending spheres. Int. J. Multiph. Flow. 75, 205–223.